

Divertor heat flux mitigation in the National Spherical Torus Experiment^{a)}

V. A. Soukhanovskii,^{1,b)} R. Maingi,² D. A. Gates,³ J. E. Menard,³ S. F. Paul,³ R. Raman,⁴ A. L. Roquemore,³ M. G. Bell,³ R. E. Bell,³ J. A. Boedo,⁵ C. E. Bush,² R. Kaita,³ H. W. Kugel,³ B. P. LeBlanc,³ D. Mueller,³ and NSTX Team

¹Lawrence Livermore National Laboratory, Livermore, California 94551, USA

²Oak Ridge National Laboratory, Oak Ridge, Tennessee 37831, USA

³Princeton Plasma Physics Laboratory, Princeton, New Jersey 08543, USA

⁴University of Washington, Seattle, Washington 98195, USA

⁵University of California at San Diego, La Jolla, California 92093, USA

(Received 6 August 2008; accepted 15 December 2008; published online 5 February 2009)

Steady-state handling of divertor heat flux is a critical issue for both ITER and spherical torus-based devices with compact high power density divertors. Significant reduction of heat flux to the divertor plate has been achieved simultaneously with favorable core and pedestal confinement and stability properties in a highly shaped lower single null configuration in the National Spherical Torus Experiment (NSTX) [M. Ono *et al.*, Nucl. Fusion **40**, 557 2000] using high magnetic flux expansion at the divertor strike point and the radiative divertor technique. A partial detachment of the outer strike point was achieved with divertor deuterium injection leading to peak flux reduction from 4–6 MW m⁻² to 0.5–2 MW m⁻² in small-ELM 0.8–1.0 MA, 4–6 MW neutral beam injection-heated H-mode discharges. A self-consistent picture of the outer strike point partial detachment was evident from divertor heat flux profiles and recombination, particle flux and neutral pressure measurements. Analytic scrape-off layer parallel transport models were used for interpretation of NSTX detachment experiments. The modeling showed that the observed peak heat flux reduction and detachment are possible with high radiated power and momentum loss fractions, achievable with divertor gas injection, and nearly impossible to achieve with main electron density, divertor neutral density or recombination increases alone. © 2009 American Institute of Physics. [DOI: 10.1063/1.3068170]

I. INTRODUCTION

Steady-state mitigation of divertor heat flux and material erosion are critical issues for both ITER and spherical torus (ST) based devices. At present, the candidate mitigation techniques are radiative (detached) divertors and specialized divertor geometry. In ITER, an H-mode discharge with small edge localized modes (ELMs, $\Delta W_{\text{ELM}}/W_{\text{plasma}} < 0.3\%$, where W is the energy) and partially detached divertor (PDD) strike points is envisioned as a baseline steady-state operation scenario¹ with a peak divertor heat flux under 10 MW m⁻², a limit imposed by the present day divertor material and engineering constrains. Particle and heat fluxes are reduced in the radiative (detached) divertor by means of volumetric momentum and energy dissipative processes—the ion-neutral elastic and inelastic collisions, recombination and radiative cooling.²

In the ST magnetic geometry access to the radiative divertor as well as its efficiency have been in question because of an inherently large divertor figure of merit P/R (Ref. 3) (where P is input power and R is major radius), and because of geometric features of the ST divertor—a small plasma volume, a small plasma-wetted area, a short parallel connection length, and a large heat flux asymmetry between the inboard and outboard scrape-off layer (SOL). Experimental studies of high power ST radiative divertors provide a basis

for future ST concept development and elucidate on the limitations of the radiative divertor concept, since its extrapolation to reactorlike fusion plasma devices has been questioned.⁴ A ST-based Component Test Facility (CTF) conceptual design employs the radiative divertor and/or mantle with high radiated power fractions to reduce divertor heat loads from the predicted 15 MW m⁻² to tolerable levels $q_{\text{peak}} \leq 10$ MW m⁻².⁵ Integration of a fusion-relevant plasma-material interface with sustained high-performance plasma operation is a key program element of the recently proposed National High-power Advanced Torus eXperiment (NHTX) concept.⁶

This paper reports on the first successful experiments to obtain significant divertor heat flux reduction in the National Spherical Torus Experiment (NSTX),⁷ simultaneously with high performance and confinement plasma characteristics in a highly shaped lower single null (LSN) configuration with a high magnetic flux expansion radiative divertor. The radiative divertor experiments are part of the SOL and divertor transport and turbulence research conducted on the NSTX.^{8,9} Access to the radiative divertor regime on NSTX was previously demonstrated in 2–6 MW NBI (neutral beam injection)-heated H-mode plasmas in a weakly shaped LSN configuration (a range of elongations $\kappa=1.8$ –2.0 and triangularities $\delta=0.40$ –0.50) using a high gas injection rate generally incompatible with H-mode confinement.^{10,11}

The paper is organized as follows: Sec. II describes NSTX facility features, diagnostics, and experimental tech-

^{a)}Paper B11.00005, Bull. Am. Phys. Soc. **52**, 21 (2007).

^{b)}Electronic mail: soukhanovskii2@llnl.gov.

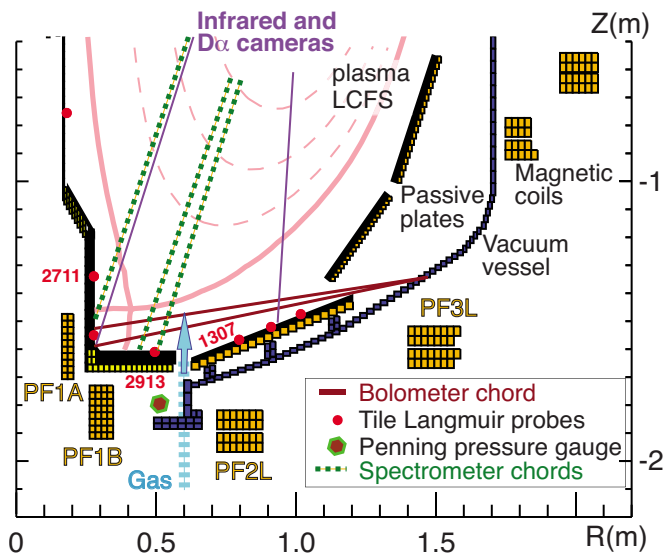


FIG. 1. (Color online) A lower part of the NSTX poloidal cross section showing the layout of divertor diagnostics, magnetic coils, and gas injectors.

niques used in the radiative divertor studies. In Sec. III A, the results of divertor detachment studies in the low κ , δ shape configuration are summarized, followed by a description of the experiments on heat flux reduction by high flux expansion divertor and detachment in highly shaped plasmas in Sec. III B. Comparisons are made where appropriate to large aspect ratio tokamak divertor experiments. The NSTX experimental results are discussed within the framework of one-dimensional analytic heat conduction and noncoronal impurity radiation models in Sec. IV. A discussion of SOL geometry and high flux expansion divertor plasma properties is presented in Sec. V.

II. EXPERIMENTAL FACILITY, DIAGNOSTICS, AND METHOD

A number of special facility and diagnostic capabilities must be realized for successful radiative divertor studies. Details of the NSTX device, diagnostics, and method are summarized in this section.

The NSTX divertor consists of horizontal and tilted ($\theta=24^\circ$) toroidally extended copper plates covered with 1.25 cm thick graphite tiles. The tiles act as plasma-facing components. The upper and lower divertor plates are symmetric. Both divertors are of open geometry enabling much flexibility in plasma shaping.

The plasma control system in NSTX enables routine attainment of high-performance highly shaped plasmas.^{12–14} The highly shaped LSN configuration with a high flux expansion divertor was obtained by creating a poloidal field null using divertor coils PF1A and/or PF1B as shown in Fig. 1. The LSN configuration had an inner strike point (ISP) on the vertical target (graphite tile covered center stack), while the outer strike point (OSP) was positioned on the horizontal divertor plate. Coil currents were controlled in a feedback mode using a real-time equilibrium reconstruction code μ EFIT (Ref. 15) to keep the X-point height nearly constant.

Deuterium gas was injected from several high-pressure computer-controlled injectors at rates $\Gamma=2.1–9.8 \times 10^{21} \text{ s}^{-1}$. For plasma refueling, both the low and the high field side midplane injectors were used. In radiative divertor experiments, a divertor gas injector equipped with a piezoelectric valve with ms-scale response was used. The gas injector orifice was situated between the lower divertor plates as shown in Fig. 1, so that deuterium was injected into the outer SOL. Midplane deuterium injections have been previously used in NSTX divertor detachment experiments.^{10,11} However, they proved to be too disruptive and often led to a H-L back transition.

To capture the complex relationship of SOL plasma and atomic processes in the radiative (detached) divertor phase, measurements at the upstream (midplane and/or X-point region) and downstream (divertor) SOL locations must be made. Plasma transport in the highly collisional SOL is described by the moments of the gyroaveraged kinetic equations for each plasma species, referred to as the Braginskii equations.¹⁶ The coordinate system is adopted with elementary vectors in the directions parallel and perpendicular to the magnetic field, and the radial direction. For the interpretation of detachment experiments, plasma transport in the direction parallel to the magnetic field x can be described by a simplified yet insightful set of one-dimensional steady-state continuity, momentum, and power balance equations (e.g., Refs. 17–19),

$$\frac{\partial(nv)}{\partial x} = n(n_n \langle \sigma v \rangle_i - n \langle \sigma v \rangle_{\text{rec}}) + S_\perp, \quad (1)$$

$$\frac{\partial(mnv^2 + 2nT)}{\partial x} = -mnv(n_n \langle \sigma v \rangle_{\text{cx+el}} + n \langle \sigma v \rangle_{\text{rec}}), \quad (2)$$

$$\begin{aligned} & \frac{\partial}{\partial x} \left(-\kappa_0 T^{5/2} + \frac{1}{2} mnv^3 + 5nTv \right) \\ & = -n^2 f_Z L_Z - \frac{3}{2} T n n_n \langle \sigma v \rangle_{\text{cx+el}} - n E_{\text{ion}} \langle \sigma v \rangle_i + Q_\perp. \end{aligned} \quad (3)$$

In the equations, n , T , and v are the plasma one fluid temperature, density, and velocity, respectively. Neutral density is denoted by n_n , impurity fraction by $f_Z = n_Z/n_e$, where Z is the nuclear charge, and impurity radiation efficiency by L_Z . Atomic process rates $\langle \sigma v \rangle$ are labeled (i) for ionization, (rec) for recombination, including both the radiative and three-body processes, and (cx+el) for charge exchange and elastic collisions. Particle and heat sources due to radial transport are labeled S_\perp and Q_\perp , respectively. Parallel SOL transport and divertor detachment will be discussed throughout the paper in the context of these equations.

The layout of NSTX edge diagnostics is shown in Fig. 1. Divertor heat flux profiles were measured by infrared microbolometer cameras operated at a 30 Hz framing rate.^{20,21} Divertor emission profiles were measured using one-dimensional CCD arrays with ms-scale spatial resolution, operated at 1–20 kHz rate. The arrays were spectrally filtered for deuterium Balmer- α (656.1 nm), Balmer- γ (433.9 nm), and/or He II Paschen- α (468.5 nm) emission

lines using $\Delta\lambda=1.0\text{--}1.5$ nm bandpass interference filters.²² A 0.5 m commercial spectrometer with three independent collimated views and a CCD detector operated at 30–100 Hz was used to monitor UV and visible spectra.²³ The filtered CCD arrays and spectrometer were photometrically calibrated *in situ* using a calibration transfer standard placed inside the NSTX vacuum vessel. The cameras and spectrometer were used to monitor the onset and extent of volume recombination during detachment. High- n Balmer series line spectra were also used to infer averaged electron density and temperature in the recombining plasma region using the Stark broadening and line intensities.²³ Radiated power was measured using silicon diode (AXUV) arrays in the core, and a four-channel gold foil bolometer system in the divertor.²⁴ Tile Langmuir probes of the flush-mounted design^{25,26} swept with ± 50 V were used for ion flux measurements using the standard I – V characteristic method for I_{sat}^+ analysis. Divertor parallel ion flux densities were obtained from current density measurements, $\Gamma_i = I_{\text{sat}}^+ A_{\text{probe}}^{-1} (e \sin \gamma)^{-1} = J_{\text{sat}}^+ (e \sin \gamma)^{-1}$, where e is the electron charge, A_{probe} is the probe area, and γ is the angle between the total magnetic field and the probe tip surface. To monitor neutral pressure, microionization and Penning gauges,²⁷ located at several midplane and divertor locations, were used. The neutral pressure measurements were not conductance-limited. Core and midplane (upstream) SOL plasma electron and ion (carbon) temperatures and densities were measured using the 30-point multipulse Thomson scattering (MPTS) system operated at 60 Hz,^{28,29} and the 20-point charge exchange recombination spectroscopy (CHERS) system,³⁰ operated at 30 Hz, respectively. Edge C III (465.0 nm line) and He II (468.5 nm line) brightness profiles were measured by the edge rotation diagnostic (ERD).³¹ The line-integrated brightnesses B_λ profiles were inverted, and local emissivities E_{exp} at the maximum brightness location were used to obtain edge C III and He II densities n_i , as follows:

$$B_\lambda = \frac{1}{4\pi} \int_l E_{\text{exp}} dl, \quad (4)$$

$$n_i = E_{\text{exp}} / \epsilon_{\text{ADAS}}(T_e, n_e), \quad (5)$$

where the MPTS T_e and n_e measurements and the corresponding photon emission coefficients ϵ_{ADAS} from a full collisional-radiative model of Atomic Data and Analysis Structure (ADAS)³² were used.

The power flowing into the SOL was estimated from measured quantities according to a conventional power accounting procedure outlined in Ref. 24,

$$P_{\text{SOL}} = P_{\text{OH}} + P_{\text{NBI}} - P_{\text{rad}} - dW/dt - P_{\text{loss}}, \quad (6)$$

where P_{OH} is the Ohmic power, P_{NBI} is the NBI power, P_{rad} is the core radiated power, and W_{MHD} and P_{loss} are the stored energy and the fast ion loss power, respectively.

III. DIVERTOR HEAT FLUX REDUCTION AND DETACHMENT

In large aspect ratio tokamaks, when SOL collisionality becomes high ($\nu_e^* \leq 60\text{--}100$), atomic processes lead to power and momentum losses at the target.² The atomic processes include line radiation (of impurity and neutrals), charge exchange, elastic, and inelastic collisions between ions and neutrals. A parallel plasma pressure loss at the divertor target (i.e., detachment) is observed, with the associated reduction of power and particle fluxes. The detachment may be only partial, occurring in the radial region adjacent to the separatrix (e.g., Refs. 33 and 34). Such PDD regime could be induced by extrinsic deuterium (e.g., Ref. 35) or impurity seeding (e.g., Refs. 36 and 37), and/or occur naturally at high plasma density.^{34,38} The detachment threshold and characteristics were found to depend on divertor geometry, target orientation, divertor pumping, and magnetic geometry.^{2,34,39,40} In particular, recent tokamak results show that the magnetic balance and the ion $B \times \nabla B$ drift direction play an important role in divertor physics.^{41–43} The present NSTX study deals with the LSN configuration with the ion ∇B drift direction toward the lower X-point. In general, the observed divertor power and particle asymmetries were consistent with large aspect ratio tokamak experiments.⁴⁴ However, characterization of the impact of radial and poloidal $E \times B$ drifts on measured magnitude and direction of SOL particle and power flows was beyond the existing NSTX facility, diagnostic and modeling capabilities, and thus outside of the present study.

In this section we describe divertor heat flux reduction and detachment studies performed in two NSTX plasma configurations described by the lower-end and higher end κ and δ . Core and pedestal plasma confinement and magnetohydrodynamic (MHD) stability properties depend on the plasma shape configuration. In the divertor LSN configuration, optimization of the shape control parameters, such as the plasma elongation κ and triangularity δ , often leads to performance improvements. Measurable differences in SOL and divertor performance were observed in NSTX between the lower-end and higher-end κ, δ configurations, drawing comparisons to large aspect ratio tokamak divertors of open geometry operated without active pumping.^{2,34,45}

A. Lower-end triangularity and elongation plasmas

Divertor heat flux reduction and detachment in NSTX were previously studied in the LSN plasmas with lower-end elongation $\kappa \approx 1.8\text{--}2.0$ and triangularity $\delta \approx 0.4\text{--}0.5$. Discharges run in this configuration were typical of the earlier years of the NSTX research program.⁴⁶ Large particle and heat flux asymmetries between inner and outer SOL regions were measured in this configuration.

The inner divertor leg detachment occurred naturally at $\bar{n}_e \approx (2\text{--}3) \times 10^{19} \text{ m}^{-3}$ and input power $0.8 \leq P_{\text{NBI}} \leq 6$ MW. The inner divertor leg region remained in a highly recombining (detached) state with $q_{\text{in}} < 1 \text{ MW/m}^{-2}$ and $T_e \leq 1.2$ eV, $n_e \approx (0.7\text{--}4) \times 10^{20} \text{ m}^{-3}$ throughout the operating space, similar to conventional tokamaks.² Inner strike point detachment was attributed to a combination of factors: the proxim-

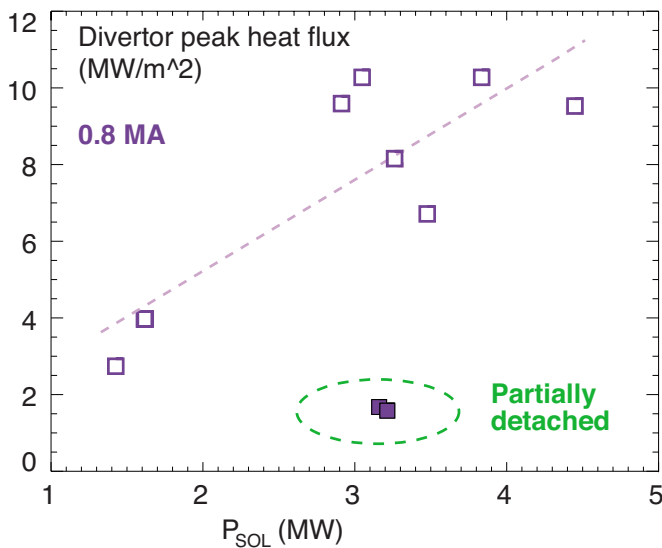


FIG. 2. (Color online) Divertor peak heat flux q_{pk} as a function of power flowing into the SOL P_{SOL} for lower-end κ, δ discharges. For comparison, also shown are the peak heat fluxes measured in discharges with a partially detached OSP.

ity of the vertical inner wall acting as a source of deuterium neutrals and carbon, a broad heat flux profile with much reduced q_{pk} , and a longer connection length.⁴⁷

The density threshold for the outer SOL detachment was found to be high, as the detachment, in general, was not observed even at the plasma densities approaching the Greenwald density n_G . In NBI-heated H-mode plasmas the outer SOL peak heat flux q_{pk} demonstrated a linear scaling with the SOL power, being in the 2–12 MW m^{-2} range for 1–6 MW NBI power. Also similar to tokamak divertor studies (e.g., Refs. 48 and 49) q_{pk} was found to increase monotonically with the plasma current I_p commensurate with the change in q_{95} and the corresponding connection length L_{\parallel} .⁵⁰ Power balance analysis typically accounted for up to 70% of P_{in} , with up to 10% radiated in the divertor²⁴ even at highest densities. It is therefore not surprising that the OSP detachment was not observed in these experiments.

Radiative divertor experiments were conducted in 4 MW NBI-heated H-mode discharges using D_2 injection at rates $\Gamma_{\text{D}_2} = 5\text{--}29 \times 10^{21} \text{ s}^{-1}$.^{10,11} A steady-state highly radiating high-recycling divertor regime and a PDD regime have been established, with the OSP heat flux reduction from $q_{pk} = 4\text{--}6 \text{ MW m}^{-2}$ to $0.5\text{--}1.5 \text{ MW m}^{-2}$. However, only the highly radiating high-recycling regime was found to be compatible with good core plasma performance and H-mode confinement. In the PDD regime, heat flux reduction, signs of volume recombination and transient reductions in divertor ion flux were measured in the OSP region. The PPD regime was obtained only at high D_2 injection rates $\Gamma_{\text{D}_2} = 15\text{--}29 \times 10^{21} \text{ s}^{-1}$ that led to an X-point MARFE formation and confinement degradation. The results of the q_{pk} reduction experiments in the lower-end κ, δ LSN configuration are summarized in Fig. 2, where q_{pk} is plotted as a function of P_{SOL} for small-ELM H-mode 0.8 MA plasmas. The limited access to detachment was found to be qualitatively consistent with

predictions of zero-dimensional two point models and two-dimensional multifluid modeling^{10,11} using the UEDGE code.⁵¹

These experiments demonstrated the difficulty in attaining adequate steady-state volumetric power and momentum loss required for detachment at high parallel heat flux $q_{\parallel} \leq 30\text{--}50 \text{ MW m}^{-2}$ in the open geometry carbon divertor with a short parallel length and poor gas entrapment typical of the lower-end κ, δ configurations. In contrast, encouraging results were obtained in a highly shaped plasma configuration discussed in the next section.

B. Highly shaped plasmas with high flux expansion divertor

Tokamak plasma performance generally improves with increased plasma shaping. A similar relation between strong shaping and high performance was demonstrated recently in NSTX in H-mode plasmas with $\kappa = 2.2\text{--}2.5$ and $\delta = 0.6\text{--}0.8$, obtained as a result of improvements in the NSTX coil design and plasma control system.^{13,14} Improved plasma performance approaching the performance level of CTF with high $\beta_t = 15\text{--}25\%$, high $\beta_N \leq 5.7$, and a high bootstrap current fraction $f_{\text{BS}} = 45\text{--}50\%$ sustained for several current redistribution times has been achieved in the highly shaped plasmas on the NSTX.^{9,13} Higher plasma shaping factor also led to longer plasma pulses, and an H-mode regime with smaller ELMs.¹³ Routine attainment of high-performance highly shaped plasmas in NSTX presented an opportunity to study divertor properties in a different geometry.

A salient feature of the highly shaped configuration is the high divertor poloidal magnetic flux expansion,

$$f_m = \frac{(B_{\theta}/B_{\text{tot}})^{\text{MP}}}{(B_{\theta}/B_{\text{tot}})^{\text{OSP}}}, \quad (7)$$

where $B_{\theta}, B_{\text{tot}}$ are the poloidal and total magnetic field at the OSP and midplane (MP) locations.⁴⁹ A higher flux expansion f_m may lead to a higher area expansion factor $A_{\text{exp}} = f_m R_{\text{OSP}}/R_{\text{MP}}$, where R is the major radius evaluated at the OSP and midplane separatrix. The area expansion factor thus accounts for the actual total area of the projection of the expanded flux tube cross section. In the highly shaped configuration the area expansion was $A_{\text{exp}} = 3.5\text{--}7.8$. This was significantly higher than the area expansion factor $A_{\text{exp}} = 2.0\text{--}2.8$ attained in discharges with lower-end κ, δ . The expansion of a heat-carrying magnetic flux tube is presently considered as a candidate technique for heat and particle flux mitigation in future fusion reactor devices.^{4,52}

As a result of flux tube expansion, heat and particle fluxes in the divertor were significantly reduced. We note, however, that the deposited fluxes were reduced due to two effects: the flux expansion and the tilt of the divertor plate with respect to the incident magnetic field. Shown in Fig. 3 are typical heat flux profiles measured in 0.8 MA H-mode discharges with 2, 4, and 6 MW NBI input power in a highly shaped LSN configuration. The heat flux profiles in Fig. 3 had a fine internal structure, possibly due to strike point splitting caused by error fields. Peak heat flux q_{pk} was 40%–60% lower than in similar plasmas with lower-end κ, δ (Fig. 2). Similar reduction factors were evident in the particle flux

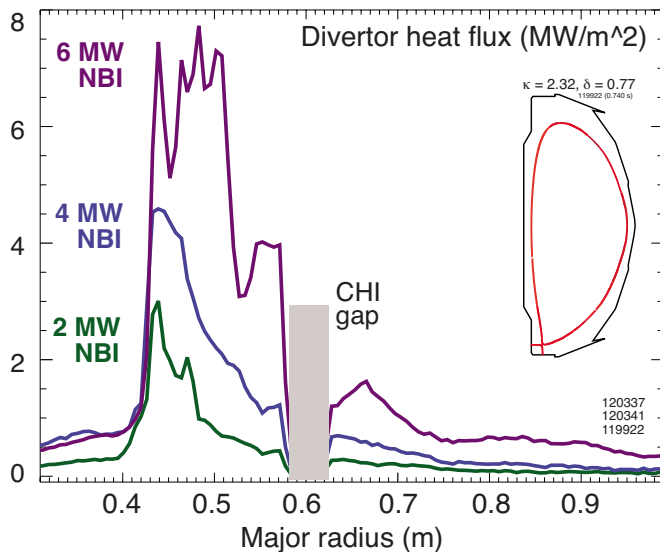


FIG. 3. (Color online) Divertor heat flux profiles in highly shaped (higher-end κ , δ) H-mode discharges at three input power values P_{NBI} .

measurements. While divertor particle flux profiles could not be measured in NSTX because of a limited spatial resolution of the Langmuir probe array (Fig. 1), single probe ion saturation currents were routinely measured in the SP region. For example, the tile Langmuir probe 2913 at $R=0.495$ m measured $j_{\text{sat}}^+ = 8\text{--}12$ A m $^{-2}$ in the OSP vicinity in the highly shaped H-mode discharges shown in Fig. 3. In the low κ and δ configuration, the tile Langmuir probe 1307 at $R=0.797$ m measured $j_{\text{sat}}^+ = 20\text{--}40$ A m $^{-2}$ in the OSP vicinity at a similar input power level.

Therefore, divertor heat and particle flux reduction comes as a natural benefit of the high-performance highly shaped ST configuration. Similar advantages of the high divertor flux expansion have been demonstrated in several large aspect ratio tokamak experiments.^{49,53,54}

C. Partially detached divertor operation in highly shaped plasmas

The high flux expansion divertor configuration, in addition to naturally reduced heat and particle fluxes, facilitates access to detachment, because of a higher radiative volume, and a possible plasma “plugging” effect counterbalancing the openness of the NSTX divertor. Experiments summarized in this section demonstrated that a partially detached divertor operation in NSTX was compatible with high core plasma performance. Experiments were carried out at three levels of input power (P_{NBI} and I_p), corresponding to a higher end of the P_{SOL} and divertor q_{pk} range. The three conditions were: 4 MW at 0.8 MA, for comparison with lower κ , δ shape results; 4 MW at 1 MA; and 6 MW at 1 MA. Partial detachment of the OSP has been obtained in all three P_{in} cases using additional divertor D $_2$ injections. We note, however, that in all three cases impurities other than intrinsic carbon were present in plasmas in small quantities. Radiation from these impurities apparently played an important role in the divertor power balance. However, detailed measurements of

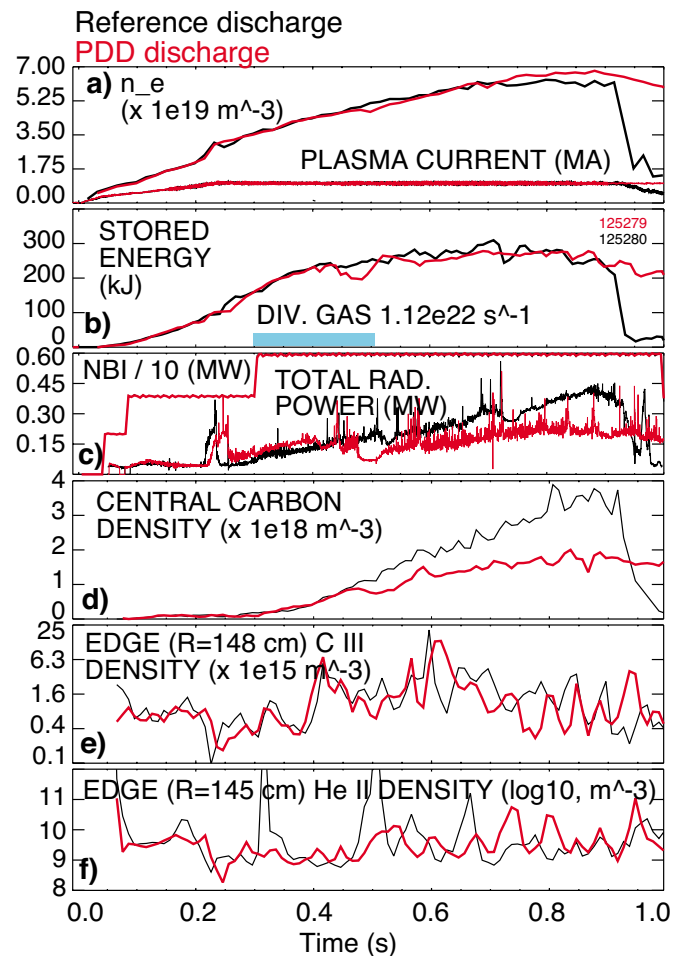


FIG. 4. (Color online) Time traces of (a) plasma current I_p , plasma density \bar{n}_e , (b) plasma stored energy W_{MHD} , divertor gas injection, (c) NBI power P_{NBI} and core radiated power P_{rad} , (d) central carbon density n_C , (e) edge C III density, (f) edge He II density, in a reference 1.0 MA, 6 MW NBI discharge and the discharge with a partially detached OSP.

these impurities were not available. Future experiments planned on the NSTX will address SOL and divertor power balance during the PDD phase.

Experiments were conducted in a highly shaped LSN configuration with $\kappa \approx 2.35$, $\delta \approx 0.83$. In this configuration, the δr_{sep} parameter, the midplane distance between the primary and the secondary separatrices, was maintained between 8 and 12 mm. The ion ∇B drift direction was toward the lower X-point, and the central toroidal magnetic field was $B_t = 0.45$ T. The core plasma conditions were: $T_e(0) \approx (0.8\text{--}1.2)$ keV, $\bar{n}_e \approx (3\text{--}5) \times 10^{19}$ m $^{-3}$. The energy confinement time in the H-mode phase was $\tau_E \approx 30\text{--}50$ ms, being in the range 1.5–1.8 of the ITER89P confinement scaling factor. In the three P_{in} cases, the H-mode plasmas had small, type V, ELMs, and occasional type I ELMs. Since the type V ELMs⁵⁵ did not carry much energy, all diagnostic measurements were averaged over several small ELMs. Large ($\Delta W/W \approx 0.10$) infrequent type I ELMs were typical of higher P_{in} discharges.

To illustrate plasma characteristics in the PDD phase, we use core, edge, and divertor measurements performed in a 1 MA, 6 MW NBI-heated H-mode discharge, with a focus

on the OSP region characterization. The inner divertor strike point typically detached in the initial part of the discharge and remained detached throughout the discharge duration, as indicated by some of the diagnostic measurements discussed in this section. However, detailed characterization of the impact of the ISP detachment on the OSP detachment, as, e.g., was done in Ref. 56, was not possible since few ISP region measurements were available.

An important result of these experiments was that core and edge plasma characteristics did not show much degradation during the PDD phase. Shown in Fig. 4 are the time traces of core and edge parameters in a reference and a PDD discharge. A transition from the high-recycling to the PDD regime occurred within 50–100 ms from the start of the deuterium pulse at 300 ms. The plasma density, stored energy, and energy confinement time changed only marginally, and the core radiated power decreased, mostly due to the core carbon concentration decrease by 30%–40%. Thomson scattering profiles showed that pedestal T_e decreased and n_e increased by 5%–10%, small enough to maintain the reference small ELM regime with $\Delta W_{\text{MHD}}/W_{\text{MHD}} \leq 1\% - 2\%$.

Intrinsic impurities play a critical role in the deuterium-seeded divertor detachment, providing a power exhaust channel via line radiation, as has been shown in large aspect ratio tokamak experiments.^{57,58} In NSTX, carbon and helium impurities were deemed important for divertor power balance in these discharges. Other impurities, e.g., boron and lithium, were present in trace quantities. The carbon source was due to chemical and physical sputtering from the divertor and main chamber plasma-facing components, while He, Li, and B remained from the helium glow-discharge cleaning,^{59,60} lithium evaporative wall conditioning experiments,⁶¹ and boronization,⁶² respectively. Carbon density measurements from CHERS indicated a reduction of core carbon concentration by up to 50% in the PDD [Fig. 4(d)] phase. In a similar manner, edge C III densities were reduced by 10%–40% in the PDD phase, being in the range 10^{15} – 10^{16} m⁻³ and corresponding to C III concentrations of $c_{\text{CIII}} \leq 0.2$ [Fig. 4(e)]. Carbon density trends in NSTX were consistent with the notion of a reduced divertor carbon source in the PDD phase. As the temperature and particle fluxes are much reduced in the OSP region during detachment, both the chemical and physical sputtering processes are drastically reduced, as has been shown in tokamaks with carbon divertor tiles.⁶³ The correlation between the PDD onset and carbon density reduction in NSTX suggested that the dominant carbon source was in the outer divertor region.

Measurements of helium density were only available in the edge region, being in the range 10^{15} – 10^{16} m⁻³ and corresponding to He II concentrations of $c_{\text{HeII}} \leq 0.05\%$ [Fig. 4(f)]. Under edge-pedestal plasma conditions ($T_e \leq 100$ eV, $n_e \approx 1 - 2 \times 10^{19}$ m⁻³) helium charge states were fairly well separated in the temperature and physical space; therefore the measured density and concentration of singly ionized helium He II were close to the total helium density in the region. Edge helium density remained unchanged during the PDD phase.

A number of SOL and divertor measurements contributed to a consistent picture of the PDD regime in the NSTX.

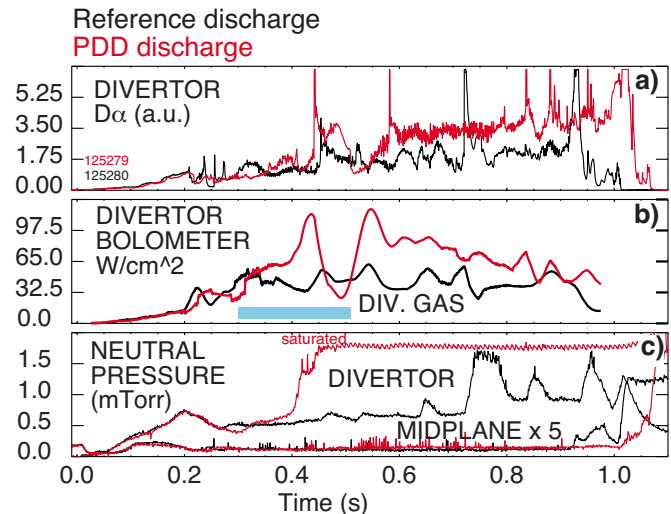


FIG. 5. (Color online) Time traces of (a) spatially integrated lower divertor D_α brightness, (b) divertor plasma brightness measured by a bolometer chord viewing the outer divertor leg, (c) midplane and divertor pressure, in a reference 1.0 MA, 6 MW NBI discharge (black traces) and the discharge with a partially detached OSP.

Shown in Fig. 5 are the time traces of local divertor-relevant quantities: the total lower divertor D_α emission, divertor bolometer chord passing through the outer leg, and neutral pressure measured in the SOL at a midplane and divertor locations. A transition to PDD was accompanied by a 50% increase in the D_α emission and divertor radiated power, as well as $\geq 75\%$ increase of divertor neutral pressure.

Power and momentum losses in the outer SOL during the PDD phase were apparent in divertor profile measurements. Heat flux profiles measured in the lower divertor region are shown in Fig. 6. The peak heat flux decreased by 50%–70% from 4–5 MW m⁻² to 1–2 MW m⁻², and the heat flux profile width increased. After the PDD onset, heat flux reduction occurred in a spatial region radially spanning $\Delta R_{\text{PDD}} \approx 10$ –15 cm, corresponding to the near SOL with

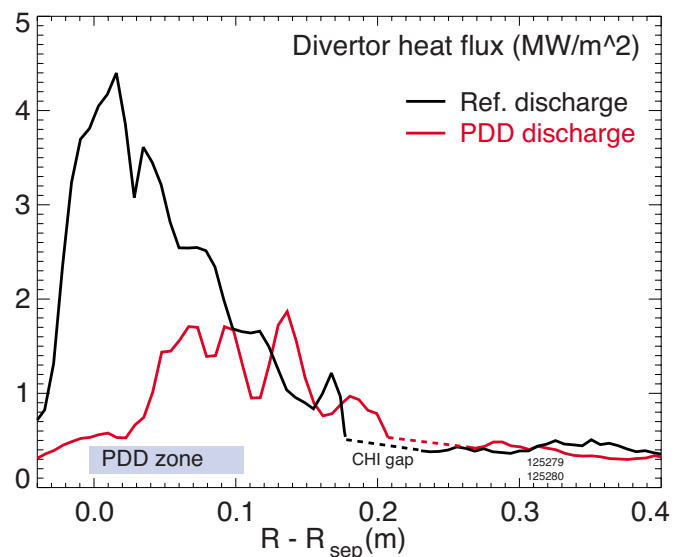


FIG. 6. (Color online) Divertor heat flux profiles in the reference 1.0 MA, 6 MW NBI discharge and the discharge with a partially detached OSP.

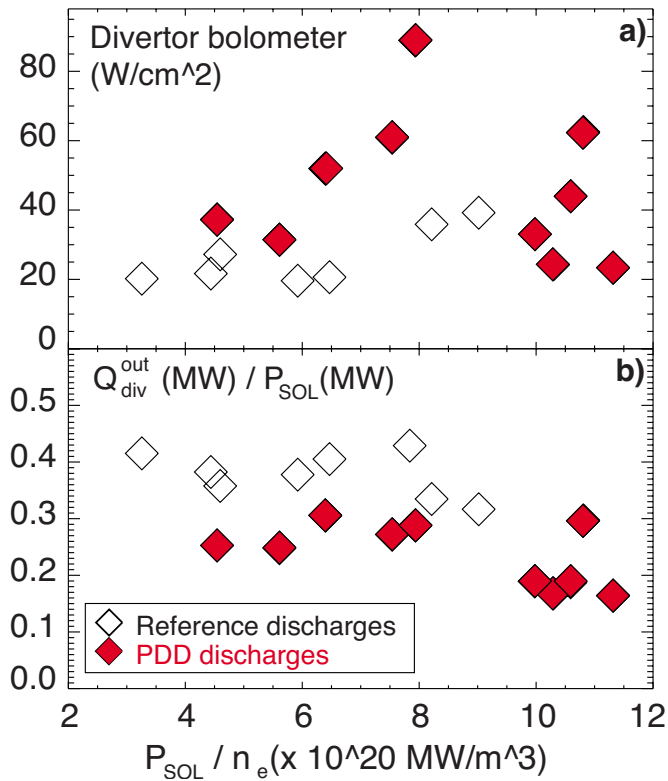


FIG. 7. (Color online) (a) Outer divertor plasma brightness (proportional to radiated power) and (b) outer divertor power fraction $Q_{\text{div}}^{\text{out}}/P_{\text{SOL}}$ as a function of SOL power per particle P_{SOL}/n_e in reference and PDD discharges.

$\Delta\psi/n \approx 0.01\text{--}0.02$ in normalized flux space. At the poloidal OSP flux expansion of 24, the PDD zone width Δr_{PDD} mapped to $\Delta_{\text{mid}} \approx 0.5\text{--}0.7$ cm in the midplane, being slightly less than the dr sep parameter (0.8–1.2 cm). Therefore, the near SOL was detached over 70%–80% in the radial extent. The heat flux profile was practically unaffected in the far SOL outside the zone of partial detachment. The infrared camera viewing the upper divertor measured negligible heat flux both prior and during the PDD phase. The q_{pk} decrease was more drastic in the 4 MW NBI, 1 MA plasmas, where a reduction from 2–2.5 MW m^{-2} to 0.5 MW m^{-2} was measured at the same D_2 injection rate.

Much of the reduction in power flowing through the SOL P_{SOL} could be attributed to the radiated power loss in the divertor. Shown in Fig. 7 are the divertor bolometer chord measurement B_{div} (a) and a relative fraction of the total power deposited in the outer divertor region Q_{div} to a total P_{SOL} (b), as functions of SOL power per particle P_{SOL}/n_e . The P_{SOL}/n_e metric is indicative of progress toward detachment. Divertor radiated power was increased up to 70% in the PDD discharges, while the relative power flowing into outer divertor in the PDD phase was reduced by 30%–50%. In the figure, a group of points with $P_{\text{SOL}}/n_e \geq 10^{21} \text{ MW m}^3$ represent the PDD discharges with lower n_e , and as a result, lower P_{rad} . A crude estimate of the total outer divertor radiated power, under the assumption of uniform distribution of radiation in the divertor leg, leads to $P_{\text{rad}} = 1\text{--}1.5$ MW for the outer divertor region. This level of the divertor radiated power, being about 30%–40% of the

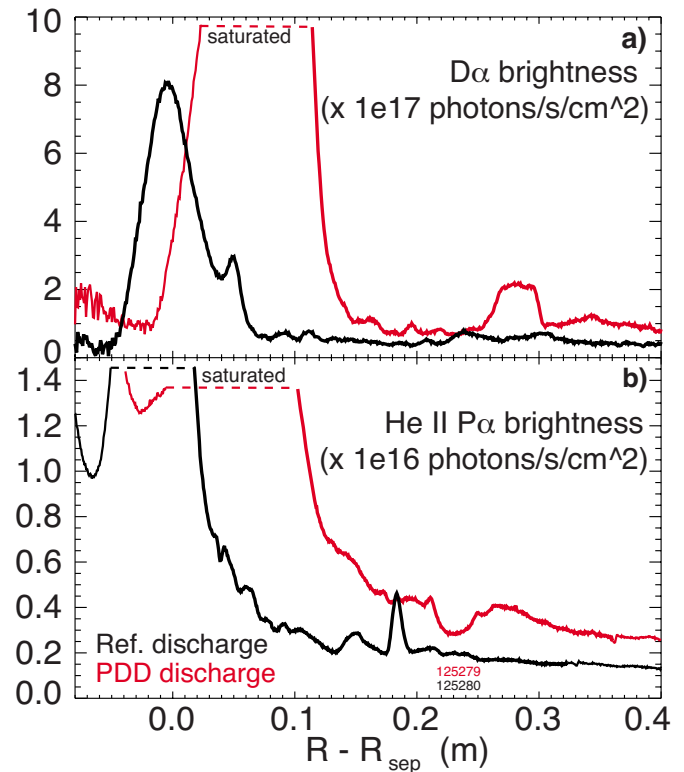


FIG. 8. (Color online) (a) Divertor $\text{D}\alpha$ and (b) $\text{He II P}\alpha$ brightness profiles in the reference 1.0 MA, 6 MW NBI discharge and the discharge with a partially detached OSP.

power flowing into the outer SOL, suggests that the observed detachment process must involve energy dissipation by charge exchange, ionization, and recombination processes.

During the PDD phase, the divertor deuterium (D I) $\text{D}\alpha$ and $\text{He II P}\alpha$ profiles also showed a substantial increase in the PDD zone, and a much lesser increase in the high-recycling zone (Fig. 8). The increase was attributed to higher photon efficiency of the $\text{D}\alpha$ and $\text{He II P}\alpha$ line emission in recombining plasmas at lower plasma temperatures and higher electron density.³² Because the large brightness increases were outside of the dynamic range of spectroscopic cameras, a detector saturation occurred, rendering a quantitative analysis in these shots difficult.

In tokamak experiments, electron-ion recombination often accompanies divertor detachment acting as an ion sink in the divertor region.^{64–66} Its signatures can be used as an experimental indicator of low T_e and increasing n_e before and during the detachment. The radiative and the three-body recombination are the dominating momentum sink process for plasma ions, although most of the momentum loss is due to the charge exchange and elastic collisions between ions and neutral atoms.^{67,68} In the NSTX experiments, a large increase in the recombination rate in the PDD phase was evident from divertor UV spectra. Shown in Fig. 9 are the UV spectra recorded along the spectrometer lines of sight (Fig. 1). The recombination rate is a strong function of temperature and density, being high $R \geq 5 \times 10^{-19} \text{ m}^3 \text{ s}^{-1}$ only when $T_e \leq 1.5$ eV and $n_e \geq 5 \times 10^{19} \text{ m}^{-3}$. The appearance and intensity increase of the Balmer lines originating in high levels $n=6\text{--}11$ indicated a strong population flux due to electron-

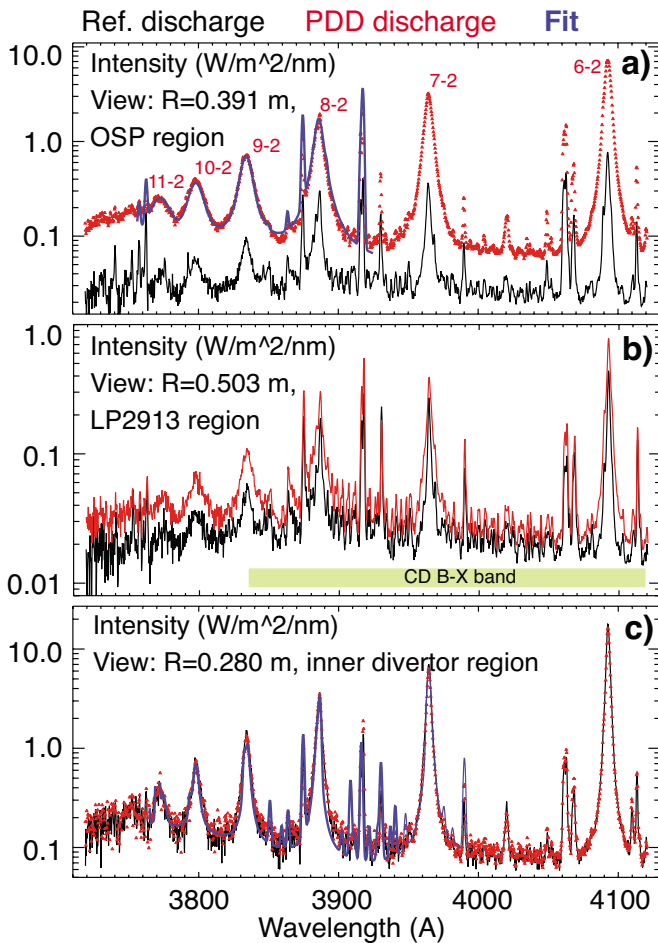


FIG. 9. (Color online) Divertor deuterium Balmer spectra recorded at three lines of sight shown in Fig. 1 in the reference 1.0 MA, 6 MW NBI discharge and the discharge with a partially detached OSP.

ion recombination processes. Based on the developed Stark broadening and line intensity analysis,²³ average plasma conditions in the PDD zone were estimated to be $n_e \leq 4 \times 10^{20} \text{ m}^{-3}$, and low $T_e \leq 1.0\text{--}1.5 \text{ eV}$ [Fig. 9(a)]. The spectrum recorded from a location marginally close to the PDD zone was indicative of a lower recombination rate and Stark broadening (lower n_e) [Fig. 9(b)]. The inner divertor region in these experiments remained in a detached state with density $n_e \leq 2\text{--}3 \times 10^{20} \text{ m}^{-3}$, evidenced by the inner divertor spectrum in Fig. 9(c), typical for H-mode NBI-heated plasmas in NSTX.⁴⁷

Divertor neutral density is a critical parameter that affects momentum loss through charge exchange and elastic ion-neutral collisions [e.g., Eq. (2)]. Geometrically closed divertors have been shown to operate at higher neutral densities than open divertors for similar \bar{n}_e , thus providing a lower detachment threshold.⁶⁹ In the lower-end κ, δ configuration in NSTX, it was possible to create high neutral pressure transiently at high gas injection rates that proved to be incompatible with H-mode confinement. In the highly shaped configuration, the situation was different. The neutral pressure time trace in Fig. 5 shows a substantial increase following the start of D_2 injection. The accuracy of these Penning gauge measurements was estimated to be $\approx 25\%$,

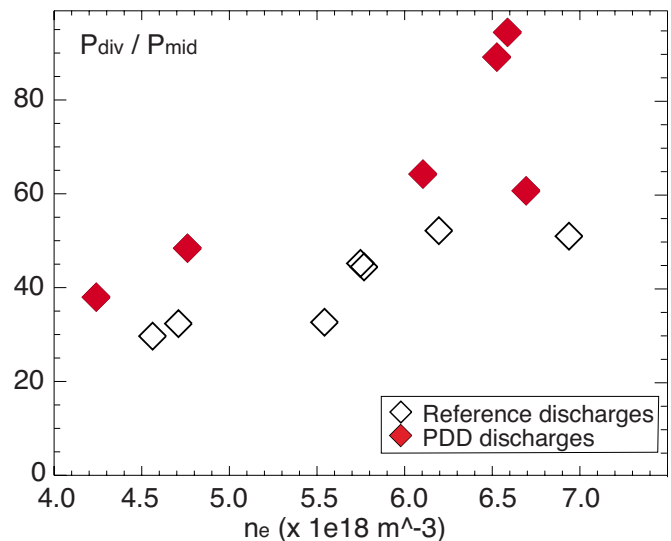


FIG. 10. (Color online) Neutral compression metric $P_{\text{div}}/P_{\text{mid}}$ as a function of plasma density \bar{n}_e in reference and PDD discharges.

and the measurement was saturated at 1.5 mTorr. Nevertheless, an estimate of the neutral compression factor $\eta = p_{\text{div}}/p_{\text{mid}}$, a ratio of pressures (densities) in the divertor chamber, and at the midplane, could be made. The comparison of $p_{\text{div}}/p_{\text{mid}}$ between reference and PDD discharges shown in Fig. 10 demonstrated that at least a 20–50% increase in the neutral compression factor was typical of the PDD discharges. The increase was mostly due to the divertor pressure increase, since midplane pressures in both cases were similar.

One of the main experimental signatures of divertor detachment in tokamaks is the Langmuir probe ion saturation current density j_{sat}^+ “rollover,” or in some cases, constant value, in the detachment zone, while the divertor D_α intensity continues to increase. This anticorrelation of j_{sat}^+ and D_α is interpreted as a decrease in the plasma particle flux to the divertor plate during the detachment, and contrasts with the sheath-limited and high-recycling regimes, where j_{sat}^+ and D_α are well correlated (see Ref. 17, and references therein). Shown in Fig. 11 are parallel ion flux density Γ_i time traces of three divertor Langmuir probes. Probe locations are shown in Fig. 1. Probe 2711, located on the vertical inner target, measured low Γ_i that did not change with gas puffing. This was consistent with the detachment of ISP and high volume recombination rate measured in the ISP region. Probe 2913 was located at 10–11 cm from the OSP, marginally in the PDD zone. Its Γ_i reduced to low, nearly constant values, during the gas injection and OSP detachment, when D_α intensity increased. This was also consistent with modest level of recombination measured at this location by spectroscopy [Fig. 9(b)]. Probe 1307 was located in the far SOL on the outer divertor plate, far from the OSP. Both j_{sat} and D_α intensity at the 1307 location increased with the gas injection, suggestive of the high-recycling conditions. Overall, Langmuir probe j_{sat} data were consistent with the PDD regime inferred from other diagnostics. The degree of detachment metric has been used for detachment characterization in tokamak experiments.³⁴ It was not possible to infer the de-

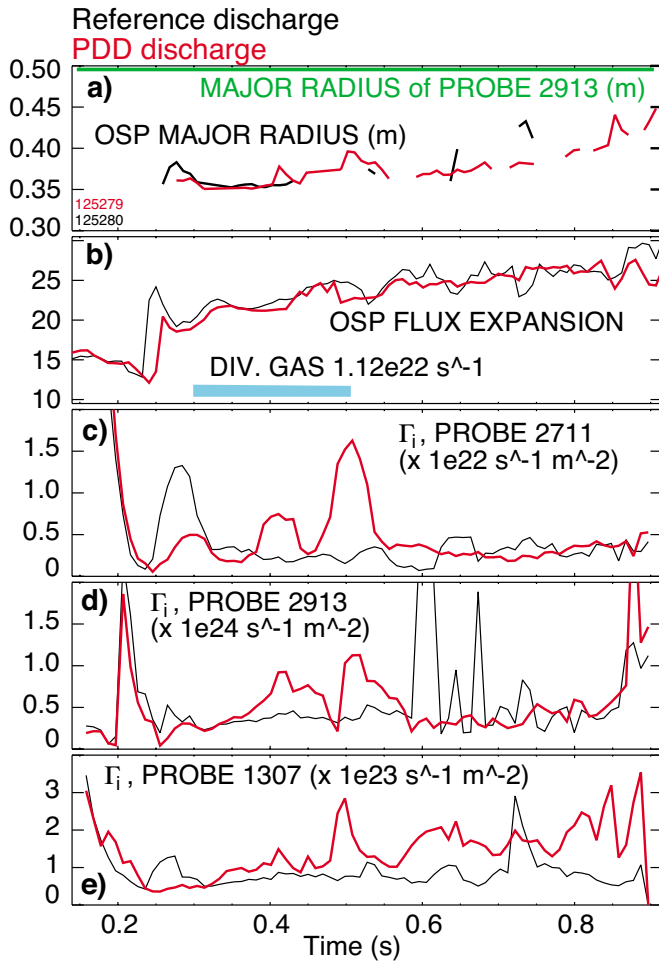


FIG. 11. (Color online) Time traces of (a) OSP major radius, (b) OSP flux expansion and divertor gas injection rate, (c) parallel ion flux Γ_i measured by inner divertor Langmuir probe 2711, (d) Γ_i measured by outer divertor Langmuir probe 2913, (e) Γ_i measured by outer divertor Langmuir probe 1307 in the reference 1.0 MA, 6 MW NBI discharge and the discharge with a partially detached OSP.

gree of detachment from Langmuir probe data in the NSTX experiments because of the SP spatial drift and core plasma density increase.

Parallel plasma momentum balance during the detachment reflects a reduction in plasma pressure due to ion-neutral friction [parallel momentum loss terms due to charge exchange and elastic collisions, Eq. (2)]. The neutral density required to explain the observed PDD regime can be estimated directly from Eq. (2), recast for convenience as

$$\frac{dp}{dx} = m\Gamma_i n_n \langle \sigma v \rangle_{\text{cx+el}} + mn^2 \langle \sigma v \rangle_{\text{rec}}. \quad (8)$$

For the SOL parameters characteristic of the discussed PDD discharges, upstream $T_e \approx 40$ eV, $n_e \approx 5 \times 10^{18} \text{ m}^{-3}$, divertor $T_e \approx 1.5$ eV, $n_e \leq 4 \times 10^{20} \text{ m}^{-3}$, and $l_x \approx 7$ m, we obtain $dp/dx = \Delta p/l_x \approx 9\text{--}10 \text{ Pa/m}$. The parallel ion flux was estimated from the Langmuir probe measurements to be $\Gamma_i \approx 3\text{--}4 \times 10^{23} \text{ m}^{-2} \text{ s}^{-1}$. Elastic collision and recombination process rates were taken as $\langle \sigma v \rangle_{\text{cx+el}} \approx 10^{-14} \text{ m}^3 \text{ s}^{-1}$ and $\langle \sigma v \rangle_{\text{rec}} \approx 10^{-18} \text{ m}^3 \text{ s}^{-1}$.¹⁷ With these numbers, an estimate of neutral density (pressure) needed to sustain the plasma pres-

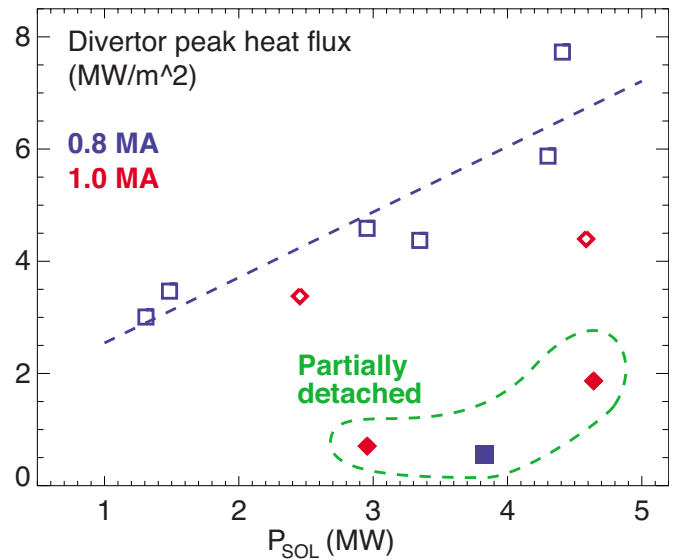


FIG. 12. (Color online) Divertor outer strike point (OSP) heat flux q_{pk} as a function of SOL power P_{SOL} for higher-end κ , δ discharges. For comparison, also shown are the peak heat fluxes measured in discharges with a partially detached OSP.

sure drop through elastic collisions and recombination was obtained from Eq. (8). If only elastic collisions were taken into account, we obtained the neutral density on the order of $n_n \approx 2.5 \times 10^{17} \text{ m}^{-3}$ and the neutral pressure $P_n \approx 1.2$ mTorr. The neutral pressure was calculated for Franck–Condon neutrals with $E=3$ eV. If the recombination sink was also taken into account, the neutral density became $n_n \approx 7 \times 10^{17} \text{ m}^{-3}$ and the neutral pressure $P_n \approx 3.3$ mTorr. Both neutral pressure values were of the same order as measured in PDD discharges, suggesting a large ion momentum loss during the OSP detachment.

The results of the divertor peak heat flux reduction experiments with radiative divertor in highly shaped plasmas are summarized in Fig. 12. Substantial reduction, up to 60%, in the peak heat flux was measured in PDD discharges with divertor deuterium injection. Qualitatively similar PDD characteristics were consistently observed in all three I_p , P_{NBI} cases with the same amount of D_2 injection. Comparison of peak heat fluxes in the lower-end and higher-end shaping configurations (Figs. 2 and 12) reveals that substantial, up to 90%, reduction could be obtained in the high flux expansion divertor operating in a PDD regime for the same amount of power flowing into the SOL region.

IV. MODEL

State-of-the-art two-dimensional codes that solve a full set of multifluid Braginskii equations [cf. Eqs. (1)–(3)] are used to model SOL and divertor transport in a realistic tokamak geometry (e.g., Refs. 70–73). The modeling of divertor detachment, however, has not been fully implemented, as it involves multiscale multidiscipline physics (e.g., Ref. 51).

A simplified one-dimensional model often provides an insightful interpretation of the experiment. Zero-dimensional two-point divertor models with losses¹⁷ and a number of one-dimensional models of varying complexity (e.g., Refs.

18, 19, and 74) are examples of such approach. In this work we have adopted a one-dimensional analytic SOL model of fronts developed in Ref. 74. The model appears to capture the essential physics of divertor detachment, although, two-dimensional effects, e.g., radiation transport and drift flows, are not included in the model. The model has been successfully applied to published divertor experimental results from large aspect ratio tokamaks, and favorably compared with a more rigorous one-dimensional numeric model.⁷⁴

A brief description of the five region heat conduction model with constant sources and sinks⁷⁴ will be given here along with the relevant SOL quantities for NSTX modeling. Analytic solutions of the simplified continuity, momentum, and power balance equations [Eqs. (1)–(3)] for five regions extending from the midplane ($x=0$) to the divertor plate ($x=x_d$) are obtained for electrons. Each region represents different atomic physics phenomena, such as, radiation, ionization, and recombination, separated in parallel coordinate and temperature. These regions are 1) the source term region, where volumetric SOL heat and particle sources Q_{\perp} and S_{\perp} are specified; 2) the conduction region; 3) the radiation front region, with a characteristic length Δ_L , specified by a temperature of maximum impurity (carbon) radiation efficiency $T_e \approx 10$ eV; 4) the ionization front region of length Δ_c , specified by $T_e \approx 4$ eV at which most neutrals are ionized; and 5) the recombination front region of length Δ_R with $T_e \leq 1.6$ eV, the temperature at which the total (three body and radiative) recombination rate of atomic deuterium exceeds the ionization rate. Electron heat conduction is assumed to be the dominant heat transport mechanism. The radiation source is defined by the radiation front region length Δ_L and magnitude L , where L/L_c is a fraction of the maximum possible impurity radiation loss L_c . Divertor neutral sources and sinks, e.g., recycling neutral source, charge exchange, and recombination sources, and neutral transport are not explicitly included; their effects are parameterized by 1) an additional particle flux Γ_0 as a fraction of the main ionization source flux $S_{\perp,x}$ corresponding to divertor “flux amplification,” 2) a specified recombination source R , and 3) a term describing the neutral friction parametrized by ion-neutral collision frequency. The latter two terms are switched on only at the divertor temperature $T_e \leq 1.5$ eV when the recombination and elastic collision processes should no longer be neglected.

The NSTX heat and particle volumetric SOL sources are estimated from the measurements. The heat source in the SOL $Q_{\perp} = P_{\text{SOL}}/V_{\text{SOL}}$, where the main SOL volume is $V_{\text{SOL}} = A_{\text{SOL}}\Delta_{\text{SOL}}$. For the low κ, δ plasmas, $A_{\text{SOL}} \approx 28$ m², whereas for the highly shaped plasmas it is $A_{\text{SOL}} \approx 32$ m². The midplane SOL heat flux width is taken as $\Delta_{\text{SOL}} \approx 0.007$ m from experiments.^{21,50} The obtained Q_{\perp} is in the range 0.5–20 MW m⁻³. The SOL ionization source is estimated using inner and outer midplane D_{α} and outer midplane neutral pressure measurements.^{22,27,75} Average ionization fluxes of $\Gamma_i \approx (0.05\text{--}50) \times 10^{22}$ s⁻¹ are obtained, with the lower end characteristic of outer SOL fluxes, and the higher end characteristic of inner wall SOL and SOL with external gas puffing.

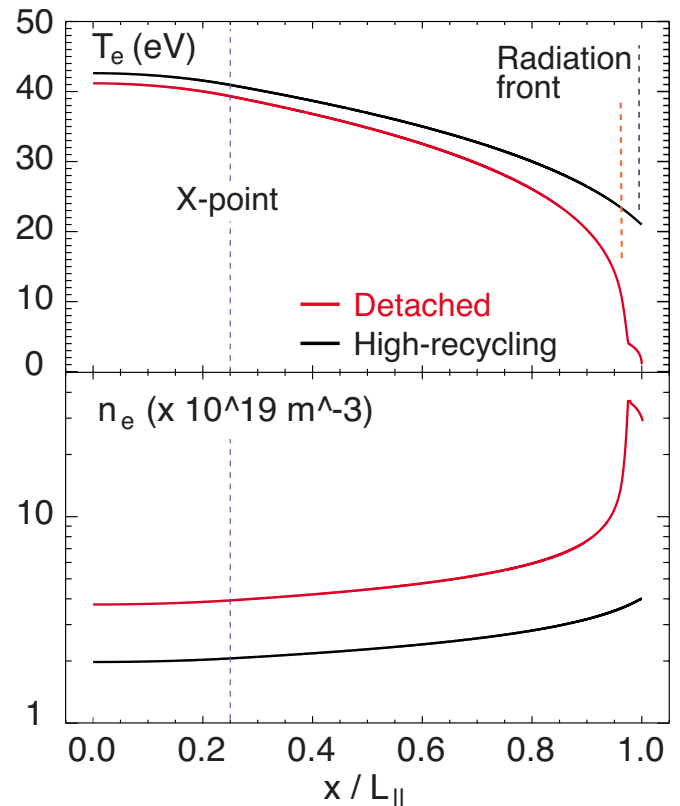


FIG. 13. (Color online) Examples of modeled T_e and n_e as functions of parallel connection length x for the attached and detached conditions. In this case, $Q_{\perp} = 10$ MW m⁻³, $S_{\perp} = 6 \times 10^{22}$ s⁻¹ m⁻³, $f_{\text{rad}} = 0.3$ (attached), $f_{\text{rad}} = 0.9$ (detached).

We use the model to obtain insight into the observed properties of NSTX divertor, namely 1) OSP detachment does not occur even at high density $\bar{n}_e \approx n_G$, 2) ISP detachment occurs at low density, 3) OSP peak heat flux reduction and detachment can be achieved only with an additional D₂ injection. The model is used to calculate parallel T_e , n_e , and v profiles for a given set of Q_{\perp} , S_{\perp} and an impurity radiated power loss fraction L/L_c . From the profiles, parallel heat flux $q_{\parallel}(x) = \kappa_0 dT_e/dx$ can also be calculated. Shown in Fig. 13 are the example profiles corresponding to an attached high-recycling case, and a detached case. The figure demonstrates that with a much increased radiated power loss term, it is possible to obtain the parallel temperature and density solution such that q_{\parallel} is very low at the plate. The T_e and n_e values are also close to the expected.

The NSTX divertor operating space can be understood using a range of Q_{\perp} , S_{\perp} and divertor f_{rad} , as shown in Fig. 14. The divertor radiated power fraction is defined as $f_{\text{rad}} = P_{\text{rad}}^{\text{div}}/q_{\parallel}^{\text{max}} = (L \times \Delta_L)/q_{\parallel}^{\text{max}}$. The detachment condition, defined as $T_e \leq 1.5$ eV, can only be achieved at the lowest input power levels, and very high divertor radiated power fractions. The SOL ionization source was $S_{\perp} = 6 \times 10^{22}$ s⁻¹ m⁻¹. This was consistent with the described observations, namely that the high-recycling conditions with $T_e^{\text{div}} \approx 5\text{--}40$ eV prevail throughout the operating space, and the OSP detachment was not observed even at high densities.

Using the standard solution in Fig. 14, we can now model different routes to detachment in NSTX. Access to

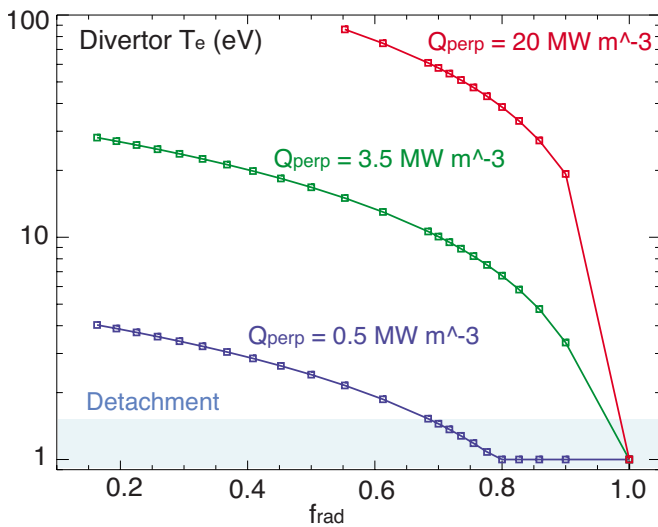


FIG. 14. (Color online) Modeled divertor T_e as a function of divertor f_{rad} for several SOL power density values Q_{\perp} . For these calculations, $\Gamma_i = 3.7 \times 10^{23} \text{ s}^{-1} \text{ m}^{-2}$ was used.

detachment is studied by 1) increasing SOL density (upstream ionization source S_{\perp}) in the model, or 2) increasing the neutral density n_n , or 3) increasing the “flux amplification” to reflect the increased divertor density and recycling due to the gas injection, or 4) increasing the divertor radiated power fraction f_{rad} , or a combination of these factors. The modeling indicated that out of the four routes, detachment conditions could be realized in NSTX mostly through the routes 3) and 4). Using route 1) alone, a substantial ionization source $S_{\perp} \geq 10^{23} \text{ s}^{-1} \text{ m}^{-3}$ was necessary to produce a detachment solution. Applying route 2) by increasing R and/or ν_i alone produced a correct trend in the density and temperature changes; however, T_e and n_e never reached the conditions for recombination onset. It is only when Γ_i was increased by 70%–90% (routes 3) and the radiated power fraction was $f_{\text{rad}} = 0.4$ – 0.8 (route 4), we obtained realistic detachment solutions for a wide range of NSTX operating parameters (Fig. 15).

A large divertor radiated power fraction appears to be a necessary condition for detachment in NSTX. We now estimate whether the large radiated power fractions can be achieved in the experiment. Here we use again a one-dimensional SOL transport model with heat conduction and noncoronal impurity radiation.⁷⁶ The model has been previously used to estimate divertor power losses for large tokamaks, such as, ITER and DIII-D.^{77,78} In the model a simplified version of Eq. (3) is integrated analytically to obtain the maximum power fraction that is possible to exhaust along x (or l_c) with conduction losses and radiated power losses due to an impurity with a fraction f_z . Noncoronal impurity radiation effects, namely, the charge exchange recombination effects and the impurity recycling effects, are parametrized in the model in terms of neutral fraction n_0/n_e and the product of electron density and impurity recycling time $n_e \tau_{\text{recy}}$, respectively. For the NSTX modeling, we used $n_0/n_e = 0.1\%$, $n_e \tau_{\text{recy}} = 10^{16} \text{ s m}^{-3}$, $T_e^{\text{sep}} = 100 \text{ eV}$, and $n_e^{\text{sep}} = 10^{19} \text{ m}^{-3}$. As shown in Fig. 16, large SOL plasma concentrations of carbon, up to 10%, are necessary to radiate a large fraction of

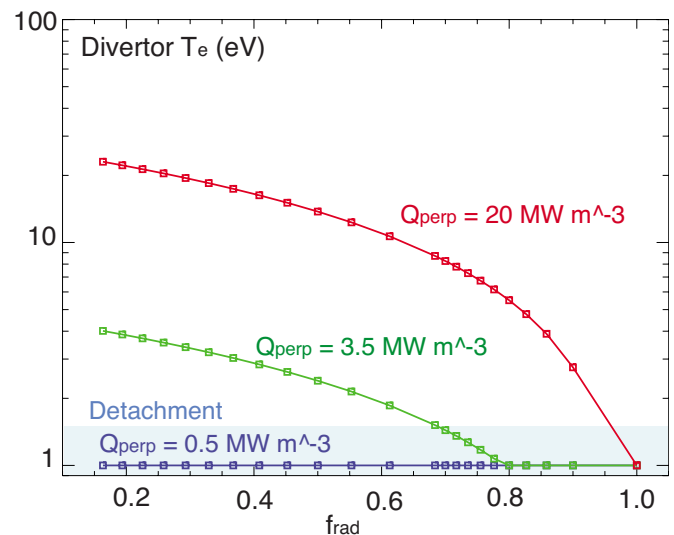


FIG. 15. (Color online) Modeled divertor T_e as a function of divertor f_{rad} for several SOL power density values Q_{\perp} , and $\Gamma_i = 3.7 \times 10^{24} \text{ s}^{-1} \text{ m}^{-2}$.

the NSTX divertor parallel heat flux $q_{\parallel} \approx 15$ – 25 MW m^{-2} , over the connection length $l_c = 8$ – 12 m . It is also evident that the presence of an additional impurity, such as, helium, would alleviate the situation, as He radiative cooling rate, particularly He II rate, is 1–2 orders of magnitude higher than that of deuterium in the 5–20 eV range.⁷⁹ Alternatively, a higher SOL electron density $n_e^{\text{sep}} \geq 10^{19} \text{ m}^{-3}$ would also significantly increase the divertor radiated power.

To summarize, it is evident that to approach highly radiative and detached conditions in the NSTX outer divertor, a large fraction of heat flux must be exhausted through radiation, and momentum loss must be substantial. These power and momentum losses are apparently achieved in NSTX only with an additional divertor gas injection. The divertor gas injection increases divertor density, recycling and radiated power. The modeling also suggests that when n_e^{SOL} (upstream ionization source) is high, while q_{\parallel} is modest,

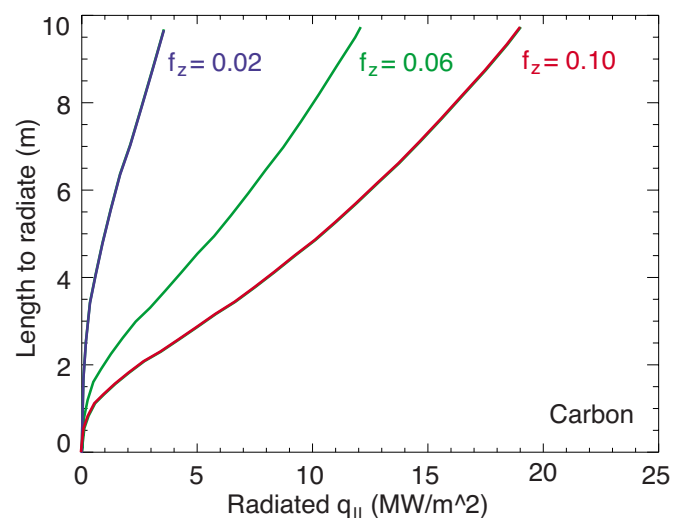


FIG. 16. (Color online) Modeled power Q_{\perp} radiated by carbon as a function of connection length for various intrinsic carbon concentrations f_z at $P_e^{\text{sep}} = 10^{19} \text{ m}^{-3}$, according to the post 1D conduction model.

TABLE I. Comparison between geometrical factors of two NSTX divertor configurations and typical large aspect ratio tokamak parameters.

Quantity	NSTX $\kappa \approx 2$ $\delta \approx 0.5$	NSTX $\kappa \approx 2.3$ $\delta \approx 0.8$	Tokamak
Aspect ratio	1.3–1.4	1.4–1.5	2.7
In-out SOL area ratio	1:3	1:3	2:3
Midplane to target connection length l_c (m)	10–12	8–10	30–80
X-point to target parallel length l_x (m)	6–8	5–7	10–20
X-point to target poloidal length l_p (m)	0.15–0.25	0.05–0.15	0.05–0.25
Poloidal magnetic flux expansion f_m at OSP	3–4	16–24	3–15
Magnetic field angle at target (degree)	12–25	2–5	1–2

the detachment can be achieved at fairly low core plasma densities, as is the case with the NSTX inner SOL and divertor.

V. DISCUSSION

We have demonstrated experimentally that significant peak heat flux reduction could be achieved in a high input power high current ST concomitantly with high core plasma performance and confinement using the radiative divertor technique. The radiative divertor was induced by a moderate-rate D₂ injection increasing radiation from intrinsic carbon and small amounts of intrinsic helium. The significance of this result is in that it was obtained in a highly shaped open divertor configuration without active pumping, suggesting that in high performance ST plasmas access to reduced divertor heat flux could be naturally facilitated by divertor geometry effects. The openness of the divertor configuration is an additional benefit since it enables much flexibility in optimization of the plasma startup and plasma shaping.

In divertor tokamak experiments, divertor geometry has a profound effect on divertor performance, heat flux reduction, and detachment operating space.⁶⁹ We briefly discuss the implications of the intrinsic NSTX SOL geometry on access to the radiative divertor regime. Shown in Table I are divertor parameters of the lower-end and higher-end κ, δ configurations discussed in Secs. III A and III B. For comparison, typical divertor parameters of a large aspect ratio tokamak, such as, DIII-D,⁸⁰ are also given. Evident from the comparison are several ST geometry features that explain the observed divertor heat flux trends in NSTX. First, a large in-out plasma surface area asymmetry in both NSTX configurations contributes to the observed differences in heat flows in the inner and outer divertor legs. Second, a relatively short parallel connection length l_x between the X-point and divertor target leads to reduced radiated power and momentum losses. As shown in Sec. IV, the fraction of q_{\parallel} that can be radiated is a strong function of l_x for the given impurity radiation function L_Z and density n_e . The momentum loss is also a function of l_x . In a shorter parallel connection length divertor, fewer ions would be able to undergo recombination processes before striking the divertor plate. This is evident when we compare electron-ion recombination time $\tau_{\text{rec}} = 1/(n_e R_{\text{rec}}) \approx 1\text{--}10$ ms to the ion residence time in the

divertor $\tau_{\text{ion}} = l_d/v_{\text{ion}} \approx 1$ ms, where R_{rec} is a total (radiative and three-body) recombination rate at $T_e \approx 1.3\text{--}1.5$ eV, and $v_{\text{ion}} \approx 10^4$ m/s is a typical thermal ion velocity.

Another notable difference between tokamaks and STs is the edge and SOL magnetic shear $\partial q/\partial\phi$. Spherical tori typically operate at edge q_{95} parameter of 6–10, i.e., much higher than in tokamaks. The angle between magnetic field lines and the divertor target α is much higher in the ST than in the large aspect ratio tokamak, leading to a higher deposited heat flux $q_{\text{div}} = q_{\parallel} \sin \alpha$ for the same parallel heat flux q_{\parallel} . The magnetic shear is also high in the SOL, leading to a large radial gradient of the parallel connection length $\partial l_x/\partial\phi$. Figure 17 illustrates the parallel magnetic field line length as a function of major radius R in the highly shaped NSTX configuration. The connection length, being relatively short in the separatrix region $l_x = 8\text{--}10$ m, becomes very short, ~ 1 m, over one SOL width λ_q in the radial direction. Since both parallel power and momentum losses are functions of l_x , a steep decline in l_x suggests that significant losses leading to the PDD regime can be sustained only in the radial region adjacent to the separatrix.

The geometric factors discussed above are similar in all NSTX LSN configurations. These factors help explain the difference observed in divertor performance trends between large aspect ratio tokamaks and STs. We now briefly discuss the factors that elucidate on the difference between the two NSTX configurations with the lower-end and higher-end triangularity and elongations. While the connection lengths in both configurations are similar, the OSP poloidal flux expansion f_m is different. When the divertor wetted area is taken into account, the area expansion factors become ≈ 2 and ≈ 6 for the plasmas with lower and higher shaping factors, respectively, explaining the observed difference in q_{pk} in Figs. 2 and 12. Other features of the high flux expansion divertor, such as, a higher isothermal divertor volume and higher plasma “plugging efficiency,” potentially lead to higher power P_{rad} and momentum p_m losses, and therefore to a natural radiative divertor regime with a lower detachment threshold. Tokamak studies conducted in open geometry unpumped graphite-tiled divertors (most relevant for comparison with NSTX)^{34,35,54,81} also support these notions. Re-ionization of recycling neutrals in the divertor chamber (also termed “flux amplification”) is an essential feature of the high-recycling

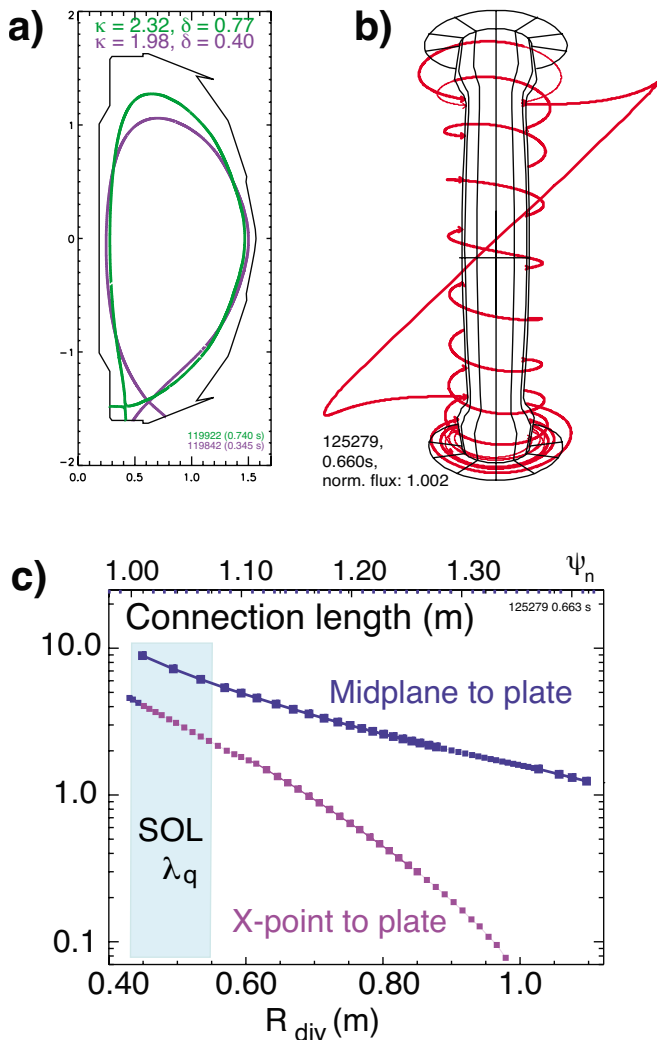


FIG. 17. (Color online) Structure of NSTX SOL flux tubes: (a) Separatrix contours of the lower-end and higher-end κ, δ configurations. (b) A visualization of the $\psi=1.002$ magnetic field line in the highly shaped configuration. (c) Connection lengths between midplane and target l_m , and X-point and target l_x , as functions of divertor major radius for the highly shaped configuration.

divertor regime. As the recycling is increased, the divertor density increases, the divertor temperature further decreases, leading to an increase in the P_{rad} and p_m loss factors, loss of parallel pressure balance, and a transition to detachment.¹⁷ The plasma “plugging efficiency” ζ is defined as a fraction of recycling neutrals re-ionized in the divertor region. In the high flux expansion divertor ζ is higher because of the large divertor plasma size in physical space in respect to ionization, charge exchange and elastic collision mean free path lengths, and higher low-temperature plasma volume.

VI. CONCLUSIONS

For the first time, the possibility of successful divertor peak heat flux mitigation in a high power density ST with a simultaneous high core plasma confinement properties has been demonstrated in NSTX using the radiative divertor technique. Divertor peak heat flux scaling developed for NSTX implies monotonic dependence on input power (and P_{SOL}) and plasma current I_p . In the highest achievable

range of $P_{NBI}=4-6$ MW and $I_p=0.8-1.0$ MA in this study, divertor peak heat flux was reduced from $4-6$ MW m^{-2} to $0.5-2$ MW m^{-2} using high magnetic flux expansion and partial detachment of the outer strike point. In combination with a very attractive small (type V) ELM high- β , high bootstrap current fraction H-mode discharge scenario this will form a basis for high-performance scenario development for future ST-based concepts.

ACKNOWLEDGMENTS

We thank T. Czeizinger, J. Desandro, R. Feder, J. Gething, L. Guttadora, J. Kukon, D. Labrie, T. Holoman, C. Priniski, T. Provost, J. Winston, B. Davis, J. Dong, D. Mastrovito, P. Roney, P. Sichta, and G. Zimmer for technical, engineering, and computer support. The NSTX team is acknowledged for plasma, NBI, and diagnostic operations.

This work was performed under the auspices of the U.S. Department of Energy in part under Contract Nos. W-7405-Eng-48, DE-AC52-07NA27344, DE-AC02-76CH03073, DE-AC05-00OR22725, W-7405-ENG-36, and DE-FG02-04ER54758.

¹D. Post, G. Janeschitz, A. Kukushkin, H. Pacher, M. Sugihara, J. Mandrekas, and W. Stacey, *Phys. Plasmas* **4**, 2631 (1997).

²ITER Physics Expert Group on Divertor, ITER Physics Expert Group on Divertor Modelling and Database, and ITER Physics Basis Editors, *Nucl. Fusion* **39**, 2391 (1999).

³K. Lackner, *Comments Plasma Phys. Controlled Fusion* **15**, 359 (1994).

⁴M. Kotschenreuther, P. Valanju, S. Mahajan, and J. Wiley, *Phys. Plasmas* **14**, 072502 (2007).

⁵Y.-K. Peng, P. Fogarty, T. Burgess, D. Strickler, B. Nelson, J. Tsai, C. Neumeyer, R. Bell, C. Kessel, J. Menard, D. Gates, B. Leblanc, D. Mikkelsen, E. Fredrickson, L. Grisham, J. Schmidt, P. Rutherford, S. Sabbagh, A. Field, A. Sykes, I. Cook, O. Mitarai, and Y. Takase, *Plasma Phys. Controlled Fusion* **47**, 263 (2005).

⁶J. Menard, R. Goldston, G. Y. Fu, N. Gorelenkov, S. Kaye, G. Kramer, R. Maingi, C. Neumeyer, S. Sabbagh, V. Soukhanovskii, and R. Woolley, in *Proceedings of the 34th EPS Conference on Plasma Physics*, edited by Z. Skladanowski and S. Wrotek (EPS, Warsaw, Poland, 2007).

⁷M. Ono, S. Kaye, Y.-K. Peng, G. Barnes, W. Blanchard, M. Carter, J. Chrzanowski, L. Dudek, R. Ewig, D. Gates, R. Hatcher, T. Jarboe, S. Jardin, D. Johnson, R. Kaita, M. Kalish, C. Kessel, H. Kugel, R. Maingi, R. Majeski, J. Manickam, B. McCormack, J. Menard, D. Mueller, B. Nelson, B. Nelson, C. Neumeyer, G. Oliaro, F. Paoletti, R. Parsells, E. Perry, N. Pomphrey, S. Ramakrishnan, R. Raman, G. Rewoldt, J. Robinson, A. Roquemore, P. Ryan, S. Sabbagh, D. Swain, E. Synakowski, M. Viola, M. Williams, J. Wilson, and N. Team, *Nucl. Fusion* **40**, 557 (2000).

⁸S. Kaye, M. Bell, R. Bell, S. Bernabei, J. Bialek, T. Biewer, W. Blanchard, J. Boedo, C. Bush, M. Carter, W. Choe, N. Crocker, D. Darrow, W. Davis, L. Delgado-Aparicio, S. Diem, J. Ferron, A. Field, J. Foley, E. Fredrickson, D. Gates, T. Gibney, R. Harvey, R. Hatcher, W. Heidbrink, K. Hill, J. Hosea, T. Jarboe, D. Johnson, R. Kaita, C. Kessel, S. Kubota, H. Kugel, J. Lawson, B. LeBlanc, K. Lee, F. Levinton, R. Maingi, J. Manickam, R. Maqueda, R. Marsala, D. Mastrovito, T. Mau, S. Medley, J. Menard, H. Meyer, D. Mikkelsen, D. Mueller, T. Munsat, B. Nelson, C. Neumeyer, N. Nishino, M. Ono, H. Park, W. Park, S. Paul, T. Peebles, M. Peng, C. Phillips, A. Pigarov, R. Pinsker, A. Ram, S. Ramakrishnan, R. Raman, D. Rasmussen, M. Redi, M. Rensink, G. Rewoldt, J. Robinson, P. Roney, A. Roquemore, E. Ruskov, P. Ryan, S. Sabbagh, H. Schneider, C. Skinner, D. Smith, A. Sontag, V. Soukhanovskii, T. Stevenson, D. Stotler, B. Stratton, D. Stutman, D. Swain, E. Synakowski, Y. Takase, G. Taylor, K. Tritz, A. Von Halle, M. Wade, R. White, J. Wilgen, M. Williams, J. Wilson, W. Zhu, S. Zweben, R. Akers, P. Beiersdorfer, R. Betti *et al.*, *Nucl. Fusion* **45**, 168 (2005).

⁹J. Menard, M. Bell, R. Bell, S. Bernabei, J. Bialek, T. Biewer, W. Blanchard, J. Boedo, C. Bush, M. Carter, W. Choe, N. Crocker, D. Darrow, W. Davis, L. Delgado-Aparicio, S. Diem, C. Domier, D.

- D'ippolito, J. Ferron, A. Field, J. Foley, E. Fredrickson, D. Gates, T. Gibney, R. Harvey, R. Hatcher, W. Heidbrink, K. Hill, J. Hosea, T. Jarboe, D. Johnson, R. Kaita, S. Kaye, C. Kessel, S. Kubota, H. Kugel, J. Lawson, B. Leblanc, K. Lee, F. Levinton, N. Luhmann, R. Maingi, R. Majeski, J. Manickam, D. Mansfield, R. Maqueda, R. Marsala, D. Mastrovito, T. Mau, E. Mazzucato, S. Medley, H. Meyer, D. Mikkelsen, D. Mueller, T. Munsat, J. Myra, B. Nelson, C. Neumeyer, N. Nishino, M. Ono, H. Park, W. Park, S. Paul, T. Peebles, M. Peng, C. Phillips, A. Pigarov, R. Pinsker, A. Ram, S. Ramakrishnan, R. Raman, D. Rasmussen, M. Redi, M. Rensink, G. Rewoldt, J. Robinson, P. Roney, A. Roquemore, E. Ruskov, P. Ryan, S. Sabbagh, H. Schneider, C. Skinner, D. Smith, A. Sontag, V. Soukhanovskii, T. Stevenson, D. Stotler, B. Stratton, D. Stutman, D. Swain, E. Synakowski, Y. Takase, G. Taylor, K. Tritz, A. Von Halle, M. Wade, R. White, J. Wilgen, M. Williams, J. Wilson, H. Yuh, L. Zakharov, W. Zhu, S. Zweben, R. Akers, P. Beiersdorfer, R. Betti, T. Bigelow, M. Bitter, P. Bonoli, C. Bourdelle, C. Chang, J. Chrzanowski, L. Dudek, P. Efthimion, M. Finkenthal, E. Fredd, G. Fu, A. Glasser, R. Goldston, N. Greenough, L. Grisham, N. Gorelenkov, L. Guazzotto, R. Hawryluk, J. Hogan, W. Houlberg, D. Humphreys, F. Jaeger, M. Kalish, S. Krasheninnikov, L. Lao, J. Lawrence, J. Leuer, D. Liu, G. Oliaro, D. Pacella, R. Parsells, M. Schaffer, I. Semenov, K. Shaing, M. Shapiro, K. Shinohara, P. Sichta, X. Tang, R. Vero, M. Walker, and W. Wampler, *Nucl. Fusion* **47**, 645 (2007).
- ¹⁰V. Soukhanovskii, R. Maingi, C. Bush, R. Raman, R. Bell, R. Kaita, H. Kugel, C. Lasnier, B. LeBlanc, J. Menard, S. Paul, and A. Roquemore, in *Proceedings of the 21st Fusion Energy Conference* (IAEA, Chengdu, China, 2006), pp. EX/P4-28.
- ¹¹V. Soukhanovskii, R. Maingi, C. Bush, R. Raman, R. Bell, R. Kaita, H. Kugel, C. Lasnier, B. LeBlanc, J. Menard, S. Paul, and A. Roquemore, *J. Nucl. Mater.* **363–365**, 432 (2007).
- ¹²D. Gates, J. Ferron, M. Bell, T. Gibney, R. Johnson, R. Marsala, D. Mastrovito, J. Menard, D. Mueller, B. Penafior, S. Sabbagh, and T. Stevenson, *Nucl. Fusion* **46**, 17 (2006).
- ¹³D. Gates, R. Maingi, J. Menard, S. Kaye, S. Sabbagh, G. Taylor, J. Wilson, M. Bell, R. Bell, S. Bernabei, J. Bialek, T. Biewer, W. Blanchard, J. Boedo, C. Bush, M. Carter, W. Choe, N. Crocker, D. Darrow, W. Davis, L. Delgado-Aparicio, S. Diem, J. Ferron, A. Field, J. Foley, E. Fredrickson, R. Harvey, R. Hatcher, W. Heidbrink, K. Hill, J. Hosea, T. Jarboe, D. Johnson, R. Kaita, C. Kessel, S. Kubota, H. Kugel, J. Lawson, B. LeBlanc, K. Lee, F. Levinton, J. Manickam, R. Maqueda, R. Marsala, D. Mastrovito, T. Mau, S. Medley, H. Meyer, D. Mikkelsen, D. Mueller, T. Munsat, B. Nelson, C. Neumeyer, N. Nishino, M. Ono, H. Park, W. Park, S. Paul, W. Peebles, M. Peng, C. Phillips, A. Pigarov, R. Pinsker, A. Ram, S. Ramakrishnan, R. Raman, D. Rasmussen, M. Redi, M. Rensink, G. Rewoldt, J. Robinson, P. Roney, L. Roquemore, E. Ruskov, P. Ryan, H. Schneider, C. Skinner, D. Smith, A. Sontag, V. Soukhanovskii, T. Stevenson, D. Stotler, B. Stratton, D. Stutman, D. Swain, E. Synakowski, Y. Takase, K. Tritz, A. Von Halle, M. Wade, R. White, J. Wilgen, M. Williams, W. Zhu, S. Zweben, R. Akers, P. Beiersdorfer, R. Betti, and T. Bigelow, *Phys. Plasmas* **13**, 056122 (2006).
- ¹⁴D. Gates, C. Kessel, J. Menard, G. Taylor, J. Wilson, M. Bell, R. Bell, S. Bernabei, J. Bialek, T. Biewer, W. Blanchard, J. Boedo, C. Bush, M. Carter, W. Choe, N. Crocker, D. Darrow, W. Davis, L. Delgado-Aparicio, S. Diem, J. Ferron, A. Field, J. Foley, E. Fredrickson, T. Gibney, R. Harvey, R. Hatcher, W. Heidbrink, K. Hill, J. Hosea, T. Jarboe, D. Johnson, R. Kaita, S. Kaye, S. Kubota, H. Kugel, J. Lawson, B. Leblanc, K. Lee, F. Levinton, R. Maingi, J. Manickam, R. Maqueda, R. Marsala, D. Mastrovito, T. Mau, S. Medley, H. Meyer, D. Mikkelsen, D. Mueller, T. Munsat, B. Nelson, C. Neumeyer, N. Nishino, M. Ono, H. Park, W. Park, S. Paul, T. Peebles, M. Peng, C. Phillips, A. Pigarov, R. Pinsker, A. Ram, S. Ramakrishnan, R. Raman, D. Rasmussen, M. Redi, M. Rensink, G. Rewoldt, J. Robinson, P. Roney, L. Roquemore, E. Ruskov, P. Ryan, S. Sabbagh, H. Schneider, C. Skinner, D. Smith, A. Sontag, V. Soukhanovskii, T. Stevenson, D. Stotler, B. Stratton, D. Stutman, D. Swain, E. Synakowski, Y. Takase, K. Tritz, A. Von Halle, M. Wade, R. White, J. Wilgen, M. Williams, W. Zhu, S. Zweben, R. Akers, P. Beiersdorfer, R. Betti *et al.*, *Nucl. Fusion* **46**, 22 (2006).
- ¹⁵J. Ferron, M. Walker, L. Lao, H. St. John, D. Humphreys, and J. Leuer, *Nucl. Fusion* **38**, 1055 (1998).
- ¹⁶S. I. Braginskii, in *Reviews of Plasma Physics*, edited by M. A. Leontovich (Consultants Bureau, New York, 1965), Vol. 1, p. 205.
- ¹⁷P. C. Stangeby, *The Plasma Boundary of Magnetic Fusion Devices* (IOP, Bristol, 2000).
- ¹⁸W. Fundamenski, P. Stangeby, and J. Elder, *J. Nucl. Mater.* **266–269**, 1045 (1999).
- ¹⁹S. Nakazawa, N. Nakajima, M. Okamoto, and N. Ohya, *Plasma Phys. Controlled Fusion* **42**, 401 (2000).
- ²⁰D. Mastrovito, R. Maingi, H. Kugel, and A. Roquemore, *Rev. Sci. Instrum.* **74**, 5090 (2003).
- ²¹R. Maingi, H. Kugel, C. Lasnier, A. Roquemore, V. Soukhanovskii, and C. Bush, *J. Nucl. Mater.* **313–316**, 1005 (2003).
- ²²V. A. Soukhanovskii, A. L. Roquemore, C. H. Skinner, D. Johnson, R. Maingi, C. Bush, F. Paoletti, and S. Sabbagh, *Rev. Sci. Instrum.* **74**, 2094 (2003).
- ²³V. A. Soukhanovskii, D. Johnson, R. Kaita, and A. L. Roquemore, *Rev. Sci. Instrum.* **77**, 10F127 (2006).
- ²⁴S. Paul, R. Maingi, V. Soukhanovskii, S. Kaye, H. Kugel, and The NSTX Research Team, *J. Nucl. Mater.* **337–339**, 251 (2005).
- ²⁵J. Gunn, C. Boucher, D. Desroches, and A. Robert, *Rev. Sci. Instrum.* **68**, 404 (1997).
- ²⁶J. P. Gunn, C. Boucher, B. L. Stansfield, and S. Savoie, *Rev. Sci. Instrum.* **66**, 154 (1995).
- ²⁷R. Raman, H. W. Kugel, R. Gernhardt, T. Provost, T. R. Jarboe, and V. Soukhanovskii, *Rev. Sci. Instrum.* **75**, 4347 (2004).
- ²⁸D. Johnson, N. Bretz, B. LeBlanc, R. Palladino, D. Long, and R. Parsells, *Rev. Sci. Instrum.* **70**, 776 (1999).
- ²⁹B. LeBlanc, R. Bell, D. Johnson, D. Hoffman, D. Long, and R. Palladino, *Rev. Sci. Instrum.* **74**, 1659 (2003).
- ³⁰R. Bell, *Rev. Sci. Instrum.* **77**, 10E902 (2006).
- ³¹T. M. Biewer, R. Bell, R. Feder, D. Johnson, and R. Palladino, *Rev. Sci. Instrum.* **75**, 650 (2004).
- ³²H. P. Summers, *The ADAS User Manual, ver. 2.6* (U. Strathclyde, Glasgow, UK, 2004), URL: <http://adas.phys.strath.ac.uk>.
- ³³T. Petrie, S. Allen, T. Carlstrom, D. Hill, R. Maingi, D. Nilson, M. Brown, D. Buchenauer, T. Evans, M. Fenstermacher, R. Jong, C. Lasnier, A. Leonard, M. Mahdavi, G. Porter, M. Wade, and W. West, *J. Nucl. Mater.* **241–243**, 639 (1997).
- ³⁴A. Loarte, R. Monk, J. Martin-Solis, D. Campbell, A. Chankin, S. Clement, S. Davies, J. Ehrenberg, S. Erents, H. Guo, P. Harbour, L. Horton, L. Ingesson, H. Jackel, J. Lingertat *et al.*, *Nucl. Fusion* **38**, 331 (1998).
- ³⁵T. Petrie, D. Hill, S. Allen, N. Brooks, D. Buchenauer, J. Cuthbertson, T. Evans, P. Ghendrih, C. Lasnier, A. Leonard, R. Maingi, G. Porter, D. Whyte, R. Groebner, R. Jong, M. Mahdavi, S. Thompson, W. West, and R. Wood, *Nucl. Fusion* **37**, 321 (1997).
- ³⁶T. Petrie, M. Wade, N. Brooks, M. Fenstermacher, M. Groth, A. Hyatt, R. Isler, C. Lasnier, A. Leonard, M. Mahdavi, G. Porter, M. Schaffer, J. Watkins, W. West, and D.-D. Team, *J. Nucl. Mater.* **363–365**, 416 (2007/06/15).
- ³⁷G. Matthews, B. Balet, J. Cordey, S. Davies, G. Fishpool, H. Guo, L. Horton, M. von Hellermann, L. Ingesson, J. Lingertat, A. Loarte, G. McCracken, C. Maggi, R. Monk, V. Parail, R. Reichle, M. Stamp, P. Stangeby, D. Stork, A. Taroni, G. Vlases, and K. Zastrow, *Nucl. Fusion* **39**, 19 (1999).
- ³⁸L. Horton, G. Vlases, P. Andrew, V. Bhatnagar, A. Chankin, S. Clement, G. Conway, S. Davies, J. de Haas, J. Ehrenberg, G. Fishpool, E. Gauthier, H. Guo, P. Harbour, L. Ingesson, H. Jackel, J. Lingertat, A. Loarte, C. Lowry, C. Maggi, G. Matthews, G. McCracken, R. Mohanti, R. Monk, R. Reichle, E. Righi, G. Saibene, R. Sartori, R. Simonini, M. Stamp, A. Taroni, and K. Thomsen, *Nucl. Fusion* **39**, 1 (1999).
- ³⁹T. Petrie, R. Maingi, S. Allen, D. Buchenauer, D. Hill, and C. Lasnier, *Nucl. Fusion* **37**, 643 (1997).
- ⁴⁰T. Petrie, N. Brooks, M. Fenstermacher, M. Groth, A. Hyatt, R. Isler, C. Lasnier, A. Leonard, G. Porter, M. Schaffer, J. Watkins, M. Wade, and W. West, *Nucl. Fusion* **48**, 045010 (2008).
- ⁴¹A. Chankin, D. Campbell, S. Clement, S. Davies, L. Horton, J. Lingertat, A. Loarte, G. Matthews, R. Monk, R. Reichle, G. Saibene, M. Stamp, and P. Stangeby, *Plasma Phys. Controlled Fusion* **38**, 1579 (1996).
- ⁴²A. Chankin, *J. Nucl. Mater.* **241–243**, 199 (1997).
- ⁴³T. W. Petrie, G. D. Porter, N. H. Brooks, M. E. Fenstermacher, J. R. Ferron, M. Groth, A. W. Hayatt, R. J. La Haye, C. J. Lasnier, A. Leonard, P. A. Politzer, M. E. Rensink, M. J. Schaffer, M. R. Wade, J. G. Watkins, and W. P. West, in *Proceedings of the 22nd Fusion Energy Conference* (IAEA, Geneva, Switzerland, 2008), pp. EX/P4-21.
- ⁴⁴R. Pitts, P. Andrew, X. Bonnin, A. Chankin, Y. Corre, G. Corrigan, D. Coster, I. Duran, T. Eich, S. Erents, W. Fundamenski, A. Huber, S. Jachmich, G. Kirnev, M. Lehnen, P. Lomas, A. Loarte, G. Matthews, J.

- Rapp, C. Silva, M. Stamp, J. Strachan, and E. Tsitrone, *J. Nucl. Mater.* **337–339**, 146 (2005).
- ⁴⁵S. Allen, N. Brooks, R. Bastasz, J. Boedo, J. Brooks, J. Cuthbertson, T. Evans, M. Fenstermacher, D. Hill, D. Hillis, J. Hogan, A. Hyatt, R. Isler, G. Jackson, T. Jernigan, C. Lasnier, R. Lehmer, A. Leonard, M. Mahdavi, R. Maingi, W. Meyer, P. Mioduszewski, R. Moyer, D. Nilson, L. Owen, T. Petrie, G. Porter, M. Rensink, M. Schaffer, J. Smith, G. Staebler, R. Stambaugh, D. Thomas, M. Wade, W. Wampler, J. Watkins, W. West, D. Whyte, N. Wolf, C. Wong, R. Wood, D.-D. Physics, and O. Teams, *Nucl. Fusion* **39**, 2015 (1999).
- ⁴⁶R. Maingi, M. Bell, R. Bell, C. Bush, E. Fredrickson, D. Gates, T. Gray, D. Johnson, R. Kaita, S. Kaye, S. Kubota, H. Kugel, C. Lasnier, B. LeBlanc, R. Maqueda, D. Mastrovito, J. Menard, D. Mueller, M. Ono, F. Paoletti, S. Paul, Y.-K. Peng, A. Roquemore, S. Sabbagh, C. Skinner, V. Soukhanovskii, D. Stutman, D. Swain, E. Synakowski, T. Tan, J. Wilgen, and S. Zweben, *Nucl. Fusion* **43**, 969 (2003).
- ⁴⁷V. Soukhanovskii, R. Maingi, C. Bush, R. Raman, R. Bell, R. Kaita, H. Kugel, C. Lasnier, B. LeBlanc, J. Menard, S. Paul, and A. Roquemore, *J. Nucl. Mater.* **337–339**, 475 (2005).
- ⁴⁸D. Hill, A. Futch, A. Leonard, M. Mahdavi, T. Petrie, D. Buchenauer, R. Campbell, J. Cuthbertson, J. Watkins, and R. Moyer, *J. Nucl. Mater.* **196–198**, 204 (1992).
- ⁴⁹C. Lasnier, D. Hill, T. Petrie, A. Leonard, T. Evans, and R. Maingi, *Nucl. Fusion* **38**, 1225 (1998).
- ⁵⁰R. Maingi, C. Bush, R. Kaita, H. Kugel, A. Roquemore, S. Paul, and V. Soukhanovskii, *J. Nucl. Mater.* **363–365**, 196 (2007).
- ⁵¹G. D. Porter, S. Allen, M. Brown, M. Fenstermacher, D. Hill, R. Jong, A. Leonard, D. Nilson, M. Rensink, T. Rognlien, and G. Smith, *Phys. Plasmas* **3**, 1967 (1996).
- ⁵²D. Ryutov, *Phys. Plasmas* **14**, 064502 (2007).
- ⁵³A. Loarte and P. Harbour, *Nucl. Fusion* **32**, 681 (1992).
- ⁵⁴R. Pitts, B. Duval, A. Loarte, J.-M. Moret, J. Boedo, D. Coster, I. Furno, J. Horacek, A. Kukushkin, D. Reiter, and J. Rommers, *J. Nucl. Mater.* **290–293**, 940 (2001).
- ⁵⁵R. Maingi, K. Tritz, E. Fredrickson, J. Menard, S. Sabbagh, D. Stutman, M. Bell, R. Bell, C. Bush, D. Gates, D. Johnson, R. Kaita, S. Kaye, H. Kugel, B. LeBlanc, D. Mueller, R. Raman, A. Roquemore, and V. Soukhanovskii, *Nucl. Fusion* **45**, 264 (2005).
- ⁵⁶M. Fenstermacher, S. Allen, D. Hill, R. Isler, C. Lasnier, A. Leonard, T. Petrie, G. Porter, W. West, D. Whyte, and R. Wood, *J. Nucl. Mater.* **266**, 348 (1999).
- ⁵⁷M. E. Fenstermacher, J. Boedo, R. C. Isler, A. W. Leonard, G. D. Porter, D. G. Whyte, R. D. Wood, S. L. Allen, N. H. Brooks, R. Colchin, T. E. Evans, D. N. Hill, C. J. Lasnier, R. D. Lehmer, M. A. Mahdavi, R. Maingi, R. A. Moyer, T. W. Petrie, T. D. Rognlien, M. J. Schaffer, R. D. Stambaugh, M. R. Wade, J. G. Watkins, W. P. West, and N. Wolf, *Plasma Phys. Controlled Fusion* **41**, A345 (1999).
- ⁵⁸R. Isler, R. Wood, C. Klepper, N. Brooks, M. Fenstermacher, and A. Leonard, *Phys. Plasmas* **4**, 355 (1997).
- ⁵⁹H. Kugel, R. Maingi, M. Bell, D. Gates, K. Hill, B. Leblanc, D. Mueller, R. Kaita, S. Paul, S. Sabbagh, C. Skinner, V. Soukhanovskii, B. Stratton, and R. Raman, *J. Nucl. Mater.* **337–339**, 495 (2005).
- ⁶⁰H. Kugel, V. Soukhanovskii, M. Bell, W. Blanchard, D. Gates, B. LeBlanc, R. Maingi, D. Mueller, H. Na, S. Paul, C. Skinner, D. Stutman, and W. Wampler, *J. Nucl. Mater.* **313–316**, 187 (2003).
- ⁶¹H. Kugel, M. Bell, R. Bell, C. Bush, D. Gates, T. Gray, R. Kaita, B. Leblanc, R. Maingi, R. Majeski, D. Mansfield, D. Mueller, S. Paul, R. Raman, A. Roquemore, S. Sabbagh, C. Skinner, V. Soukhanovskii, T. Stevenson, and L. Zakharov, *J. Nucl. Mater.* **363–365**, 791 (2007).
- ⁶²C. Skinner, H. Kugel, R. Maingi, W. Wampler, W. Blanchard, M. Bell, R. Bell, D. Gates, S. Kaye, P. LaMarche, B. LeBlanc, J. Menard, D. Mueller, H. Na, N. Nishino, F. Paoletti, S. Paul, S. Sabbagh, V. Soukhanovskii, and D. Stutman, *Nucl. Fusion* **42**, 329 (2002).
- ⁶³D. Whyte, W. West, C. Wong, R. Bastasz, J. Brooks, W. Wampler, N. Brooks, J. Davis, R. Doerner, A. Haasz, R. Isler, G. Jackson, R. Macaulay-Newcombe, and M. Wade, *Nucl. Fusion* **41**, 1243 (2001).
- ⁶⁴R. Isler, G. McKee, N. Brooks, W. West, M. Fenstermacher, and R. Wood, *Phys. Plasmas* **4**, 2989 (1997).
- ⁶⁵J. Terry, B. Lipschultz, A. Pigarov, S. Krashennnikov, B. LaBombard, D. Lumma, H. Ohkawa, D. Pappas, and M. Umansky, *Phys. Plasmas* **5**, 1759 (1998).
- ⁶⁶G. McCracken, M. Stamp, R. Monk, A. Meigs, J. Lingertat, R. Prentice, A. Starling, R. Smith, and A. Tabasso, *Nucl. Fusion* **38**, 619 (1998).
- ⁶⁷D. Lumma, J. Terry, and B. Lipschultz, *Phys. Plasmas* **4**, 2555 (1997).
- ⁶⁸C. Pitcher, J. Goetz, B. LaBombard, B. Lipschultz, J. Weaver, and B. Welch, *J. Nucl. Mater.* **266**, 1009 (1999).
- ⁶⁹A. Loarte, *Plasma Phys. Controlled Fusion* **43**, 183 (2001).
- ⁷⁰T. Rognlien, *Plasma Phys. Controlled Fusion* **47**, 283 (2005).
- ⁷¹A. Kallenbach, Y. Andrew, M. Beurskens, G. Corrigan, T. Eich, S. Jachmich, M. Kempenaars, A. Korotkov, A. Loarte, G. Matthews, P. Monier-Garbet, G. Saibene, J. Spence, and W. Suttrop, *Plasma Phys. Controlled Fusion* **46**, 431 (2004).
- ⁷²A. Chankin, D. Coster, R. Dux, C. Fuchs, G. Haas, A. Herrmann, L. Horton, A. Kallenbach, M. Kaufmann, C. Konz, K. Lackner, C. Maggi, H. Muller, J. Neuhauser, R. Pugno, M. Reich, and W. Schneider, *Plasma Phys. Controlled Fusion* **48**, 839 (2006).
- ⁷³D. Coster, X. Bonnin, G. Corrigan, G. Kirnev, G. Matthews, and J. Spence, *J. Nucl. Mater.* **337–339**, 366 (2005).
- ⁷⁴R. Goswami, P. Kaw, M. Warrier, R. Singh, and S. Deshpande, *Phys. Plasmas* **8**, 857 (2001).
- ⁷⁵V. A. Soukhanovskii, R. E. Bell, C. Bush, R. Kaita, H. W. Kugel, B. P. LeBlanc, R. Maingi, R. Raman, A. L. Roquemore, and the NSTX Research Team, "On the secular density rises in NBI-heated H-mode plasmas in NSTX," *J. Nucl. Mater.* (in press).
- ⁷⁶D. Post, N. Putvinskaya, F. Perkins, and W. Nevins, *J. Nucl. Mater.* **220–222**, 1014 (1995).
- ⁷⁷R. Clark, J. Abdallah, and D. Post, *J. Nucl. Mater.* **220–222**, 1028 (1995).
- ⁷⁸D. Post, J. Abdallah, R. Clark, and N. Putvinskaya, *Phys. Plasmas* **2**, 2328 (1995).
- ⁷⁹M. Goto, K. Sawada, and T. Fujimoto, *Phys. Plasmas* **9**, 4316 (2002).
- ⁸⁰J. Luxon, *Nucl. Fusion* **42**, 614 (2002).
- ⁸¹A. Loarte, *J. Nucl. Mater.* **290–293**, 805 (2001).